

Chapter 2

Cassegrain AO Facility

The Cassegrain AO facility of iRobo-AO[78] measures and corrects the wavefront distortions introduced including atmospheric dispersion correction. The entire facility is mounted at the main Cassegrain focus of the IUCAA 2 m telescope at IUCAA Girawali Observatory (Fig. 2.1), near Pune, India. It works in both visible as well as near infra-red bands. The wavefront measurement is done using a UV Laser Guide Star (LGS). The LGS system is described in the next Chapter. The AO facility primarily consists of three arms: two science arms working in the visible and near infra-red (NIR) and a wavefront sensing UV arm. The entire optical relay system is shown in Fig. 2.4. It mainly consists of five off-axis parabolic (OAP) mirrors, a deformable mirror (DM), a tip-tilt correcting mirror (TTM), a pair of rotating prisms used as atmospheric dispersion corrector (ADC) and two dichroic filters to split up the light into various bands. The ADC is detailed in Chapter 4. Apart from these it also has an Electron Multiplying Charged Couple Device (EMCCD) camera, a fast readout UV sensitive wavefront sensing CCD39 camera and a near infra-red camera (NIR camera) details of which is presented in Chapter 5. The dimension of the entire Cassegrain box is $1m \times 0.8m \times 0.2m$. In this chapter, the design, description and development with laboratory test results are presented of the entire AO facility.

2.1 Design

At first, the summery of the system requirements are given here.



FIGURE 2.1: IUCAA Girawali Observatory (IGO), near Pune, India.

- iRobo-AO should have the observational capability in the visible, near infrared (NIR, $1.1 - 2.5 \mu m$) domain, i.e. there will be a visible science camera and a NIR camera.
- It should provide good Strehl ratio in H, K band around $\sim 40\%$.
- The wavefront error measurement should be done by a Laser Guide Star (LGS) at high speed. From a cost perspective, Rayleigh scattered LGS using UV laser may be employed.
- Tip-tilt correction must be done by Natural Guide Star (NGS). During science observation in the visible camera, the NIR camera can work as a tip-tilt camera and vice versa.
- During the observation, the AO operation must be efficient, autonomous and robust.

2.1.1 Specific Requirements of the components

TABLE 2.1: AO System Design Parameters.

| Parameter | Description/Value |
|---|---|
| Telescope (D_{pupil}) | 2 m (IUCAA Girawali Observatory) |
| Visible | 0.4-0.9 μm |
| NIR | 1.1-2.5 μm |
| Seeing at IGO at at 0.55 μm at zenith | 1.2'' |
| Fried Parameter at 0.55 μm at zenith | 9.45 cm |
| Fried parameter r_0 for IGO - at zenith angle $z = 45^\circ$ at 355 nm | 45 mm |
| Conjugation layer | Ground layer, Telescope pupil |
| Guide star: | |
| High order aberration | LGS (Rayleigh type at $\lambda = 0.355 \mu\text{m}$) |
| Low order aberration/ tip-tilt correction) | NGS |
| Wavefront sensing | 0.355 μm |
| LGS SNR | 18.43 (343 photon/subaperture/msec) |
| Fast Steering Mirror | ± 26.2 mrad |
| Subaperture diameter (d) | 181.81 mm ($d \approx 4r_0$) |
| Telescope Simulator | UV and Visible |
| Reconstruction Method | Modal |
| Actuator Geometry | Fried Configuration |
| Optical quality: | |
| Field of view | $\sim 30''$ in visible (0.4 -0.9 μm) and $\sim 1'$ in NIR |
| Wavefront sensor: | |
| WFS type | Shack-Hertmann |
| Number of subapertures | 11×11 |
| WFS Detector | Quadcell, Fast CCD, rapid readout by 4 amplifiers |

2.1.1.1 Number of subaperture and size

A wavefront derivative type wavefront front sensor (WFS) like Shack-Hartmann WFS measures the slope of the wavefront at each subaperture¹. An LGS is used for high order wavefront measurement. However since the LGS does not probe atmospheric tip-tilt, natural guide star (NGS) is used to measure tip-tilt. The wavefront phase error variance apart from the tip-tilt is given by Noll [27],

$$\Delta_2(\text{rad}^2) = 0.134 \left(\frac{d}{r_0} \right)^{\frac{2}{3}} \quad (2.1)$$

where d and r_0 are the subaperture size and Fried Parameter respectively. Δ_2 becomes 1 rad^2 when $d \approx 3.34r_0$, which does not produce speckle. Hence the centroid detection can be done easily to measure the wavefront slope at the subaperture at the minimum number of subapertures. The size and number of subapertures can be considered as $\approx 4 r_0$ and $(D_{\text{pupil}}/4r_0)^2$ respectively.

Thus the number and size of subapertures for IGO 2m telescope are 11×11 and 181.81 mm at the $0.355 \mu\text{m}$ wavefront sensing wavelength under $r_0 = 45 \text{ mm}$ atmospheric condition (under $1.2''$ seeing at IGO at $0.55 \mu\text{m}$ at zenith, corresponds to $r_0 = 45 \text{ mm}$, at zenith angle $z = 45^\circ$, at 355 nm).

2.1.1.2 Wavefront Sensor

Thus from the discussion of section 2.1.1.1, we have used an 11×11 array of lenslets as part of the Shack-Hartmann WFS.

2.1.1.3 WFS and the DM actuator geometry

The wavefront reconstruction depends on the relation between the location of actuators (nodes/phase points) of a deformable mirror and the subaperture of Shack-Hartmann wavefront sensor. There are few geometries of SHWFS, and the actuators are used in adaptive optics system such as Modified Hudgin, Southwell, Fried, Hermann etc. A few of them are explained here [3, 49] and given in Figure 2.2.

In the Modified Hudgin, nodes are at the center of each side of subapertures.

¹The entire telescope aperture (primary mirror), i.e. pupil is divided into subapertures.

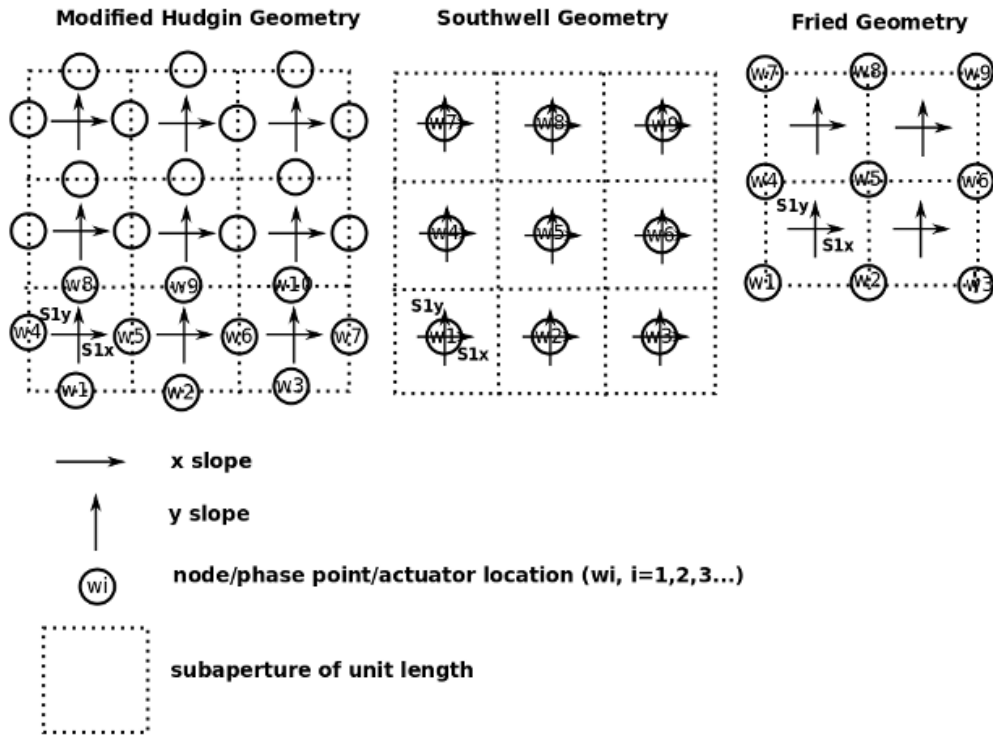


FIGURE 2.2: Geometry of subapertures and actuators

In Southwell configuration, all the subapertures are centered on the nodes. The nodes are at each corner of each subaperture in Fried configuration. The slope measurements (S_{ix} and S_{iy} are the i^{th} x and y slope respectively, where $i=1,2,\dots$) in those geometry configurations are given in Equation 2.2 from the Figure 2.2. Fried Geometry is used here as it suits our hardware, and it is well-understood geometry.

$$\text{Modified Hudgin, } S_{1x} = (w_5 - w_4), \quad S_{1y} = (w_9 - w_1)$$

$$\text{Southwell, } (S_{1x} + S_{2x})/2 = (w_2 - w_1), \quad (S_{4y} + S_{1y})/2 = (w_4 - w_1) \quad (2.2)$$

$$\text{Fried, } S_{1x} = (w_5 + w_2) - (w_1 + w_4), \quad S_{1y} = (w_4 + w_5) - (w_1 + w_2)$$

2.1.1.4 Deformable Mirror

The basic parameter of a wavefront corrector is the number of actuators /degrees of freedom within the active area of the pupil. The number of actuators needed is proportional to $(D/r_0)^2$. Fitting error is inversely proportional to the number of

degrees of freedom in the wavefront compensator. The complexity of an adaptive optics system is roughly proportional to the number of actuators or degrees of freedom, as given by [3]. There is a trade-off between complexity and fitting error (explained in section 2.1.2). The Fried configuration expects 12×12 number of actuator array for 11×11 lenslet array of WFS as per Figure 2.2.

The atmospheric turbulence demands a stroke size of (Eqn. 5 [44]),

$$\delta = \frac{3\lambda}{2\pi} \sqrt{l} \left(\frac{D_{pupil}}{r_0} \right)^{5/6} \quad (2.3)$$

where $l = 1.03$ if the DM compensates for the tip-tilt plus higher order aberrations and is equal to 0.134, if tip-tilt is separately accounted for and removed, say by using the TTM. D_{pupil} represents the telescope entrance pupil diameter. It can be seen that as r_0 varies as $\lambda^{6/5}$ the DM stroke is wavelength independent.

At IGO for $r_0 \approx 7.6$ cm at $0.550 \mu\text{m}$ at zenith angle 45° under $1.2''$ seeing, the net stroke required for complete aberration correction is $\approx 4 \mu\text{m}$ and without the tip-tilt correction $1.5 \mu\text{m}$. In Robo-AO, we use a separate tip-tilt mirror for the low order tip-tilt correction in the AO-corrected light path. Thus the required DM should have a 12×12 actuator array and $\approx 1.5 \mu\text{m}$ stroke length.

2.1.1.5 Tip-Tilt Mirror

The presence of a natural guide star however is a must for tip-tilt correction. The laser guide star cannot be used for this purpose because, after the two-way travel of laser light through the atmosphere, the tip-tilt information is lost. The high order aberration measurement is done by the LGS photons collected by the subaperture. On the other hand, all the photons collected by the entire aperture from the natural guide star are used for tip-tilt correction. Thus natural guide star fainter than the laser guide star can be used for the tip-tilt measurement. Hardy[3] gives the overall one axis tilt variance.

$$\alpha_{tilt}^2 = 0.184 \left(\frac{\lambda}{D_{pupil}} \right)^2 \left(\frac{D_{pupil}}{r_0} \right)^{\frac{5}{3}} \text{rad}^2 \quad (2.4)$$

The net angular tilt considering ± 3 sigma variation will be $\approx 11 \mu\text{radian}$ for IGO parameters, this is the overall tilt of the wavefront in one axis at the primary mirror. With an angular magnification of the beam at the TTM of ≈ 95 (as

per Zemax design), the overall atmospheric tilt after magnification at TTM will be ≈ 1 mradian. Thus a dynamic range of ≈ 1 mradian is needed for tip-tilt compensation under $1.2''$ atmospheric seeing².

2.1.1.6 Fast Steering Mirror (FSM)

Beam Pointing Drift angle is $< 10 \mu\text{rad}/^{\circ}\text{C}$, and the Pointing Drift over 8 hours full angle is $< 50 \mu\text{rad}$. Due to the pointing drift and mechanical errors, LGS does not stay at the center on SHWFS even in the absence of turbulence. To overcome this tilt a Fast Steering Mirror (FSM 300B from Newport with ± 26.2 mrad) is provided in the laser projector (given in Chapter 3) assembly. The mirror is coated especially for 355 nm laser.

2.1.2 Error budget of an LGS AO system

An error budget is prepared including high and low order aberrations for the estimation of the expected performance of iRobo-AO. It includes the Beacon Measurement error, Fitting error, error Due to Servo Lag, error due to cone effect, error Due to Anisoplanatism and errors low order aberrations (tilt temporal error, tilt anisoplanatic error). The error budget is given in Table 2.2 towards zenith. We have considered $1.2''$, typical seeing for this calculation. All these errors are added in quadrature [3].

Refractive index structure co-efficient We have taken Hufnagel model[3] to determine C_N^2 (Eqn. 2.5) and calculate Fried parameter, Isoplanetic angle, diameter of the aperture over which the wavefront error due to focal anisoplanatism is 1 rad^2 .

$$C_N^2 = B \exp\left(-\frac{h}{H_B}\right) + C h^{10} \exp\left(-\frac{h}{H_c}\right) \quad (2.5)$$

$$B = 27 \times 10^{-17}, H_B = 1500 \text{ m}, C = 5.94 \times 10^{-53}, H_c = 1000 \text{ m}$$

² $r_0=7.6$ cm at 45° zenith angle at $0.55 \mu\text{m}$.

We have adjusted the parameters of the Hufnagel model ($B = 45 \times 10^{-17}$ and $C = 6.99 \times 10^{-53}$) to get 1.2'' seeing.

Mean square wavefront phase error in a laser guide star system is expressed as the sum of error variance produced from different sources.

$$\sigma_W^2(rad^2) = \sigma_{BM}^2 + \sigma_{BT}^2 + \sigma_{Fit}^2 + \sigma_{FA}^2 + \sigma_A^2 + \sigma_{TT}^2 + \sigma_{TA}^2 \quad (2.6)$$

Each terms in the above equation is explained below.

- **Wavefront Fitting Error, σ_{Fit}^2 :**

Wavefront fitting error captures the limitation of wavefront correction by the Deformable mirror and is expressed as,

$$\sigma_{Fit}^2 = a_F \left(\frac{d}{r_0} \right)^{\frac{5}{3}} \quad (2.7)$$

where d is subaperture of value 181.81 mm of iRobo-AO and a_F is 0.3 (this may vary from 0.28 to 0.34). The Fried parameter (r_0) is given in Equation 1.3.

- **Temporal Error, σ_{BT}^2 :**

The time delay between the wavefront measurement and correction introduces the temporal error or servo lag in the feedback loop error. It is expressed as[3],

$$\sigma_{BT}^2 = k \left(\frac{f_g}{f_s} \right)^{\frac{5}{3}} \quad (2.8)$$

where f_s is the servo bandwidth of the system (800 Hz for iRobo-AO) and f_g is the characteristics frequency of the atmospheric turbulence called Greenwood frequency. The value of K is 1 in RC network when the bandwidth is defined at the half-power point. Greenwood frequency is expressed as,

$$f_g = \left[0.102k^2 secz \int C_N^2(h)v(h)^{5/3} dh \right]^{3/5}, \quad (2.9)$$

The Greenwood frequency also may be expressed as below in a particular case of single-layer turbulence with wind speed v .

$$f_g = 0.42 \left(\frac{v}{r_0} \right) \quad (2.10)$$

- **Beacon Measurement Error, σ_{BM}^2 :**

Shack-Hartmann wavefront sensor measures the slope of the wavefront by calculating the shifts of the centroid of the beacon spots at its back focal plane. The error associated with the centroid measurement strongly depends on the brightness and angular size of the LGS. The brightness of the LGS determines the signal-to-noise ratio of the detected signal. This error related to LGS measurement is called beacon measurement. It is represented as,

$$\sigma_\phi(\text{rad}) = \frac{\pi^2 K_g}{4SNR} \left[\left(\frac{3d\lambda_s}{2r\lambda_c} \right)^2 + \left(\frac{\theta d}{\lambda_c} \right)^2 \right]^{1/2} \quad (2.11)$$

where λ_s and λ_c are sensing and correcting wavelength respectively. The values of K_g typically lies within 1.2 -1.5 and 1.5 is used here.

- **Error due to angular anisoplanatism, σ_A^2 :**

The anisoplanatic error comes into play when the wavefront measurement is done with a reference source which is displaced by say angle θ , from the target star. It is given by [3],

$$\sigma_A^2 = \left(\frac{\theta}{\theta_0} \right)^{\frac{5}{3}} \quad (2.12)$$

where θ_0 is isoplanetic angle (Equation 9.24 of Hardy[3]).

- **Cone or focal anisoplanatic error, σ_{FA}^2 :**

Cone or focal anisoplanatism error is due to the finite height of laser beacon. For D_{pupil} diameter telescope it is measured by [3],

$$\sigma_{FA}^2 = \left(\frac{D_{pupil}}{d_0} \right)^{\frac{5}{3}} \quad (2.13)$$

where d_0 is the aperture over which focal anisoplanatism error remains within 1 rad^2 (Equation no 7.36 [3]).

- **Atmospheric dispersion (multi spectral error), σ_D^2 :**

It can be seen from Figure 2.3 that the residual atmospheric dispersion after correction by atmospheric dispersion corrector (see chapter 4) is around 3 mas for 0.5° prism angle off. The accuracy of the prism angle is in milli

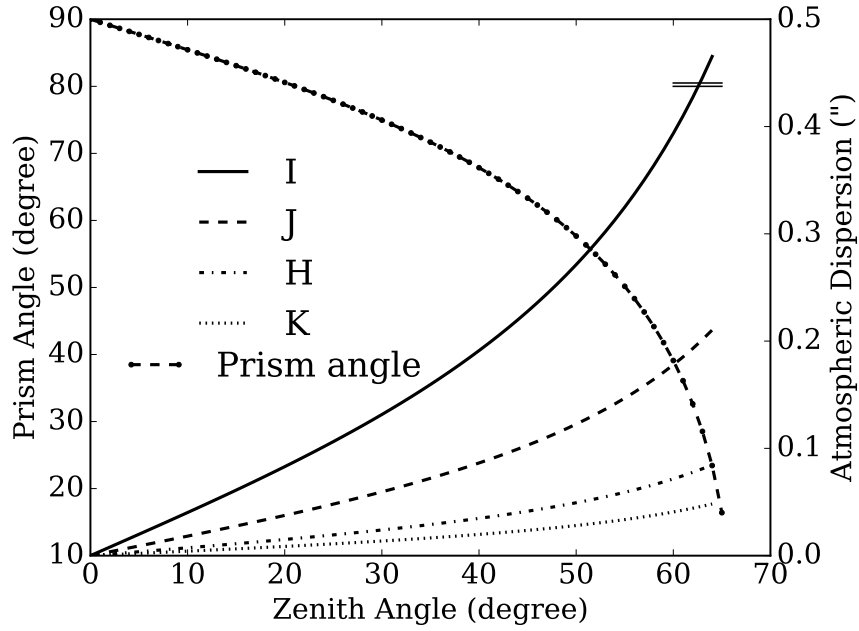


FIGURE 2.3: Band wise atmospheric dispersion and the required prism angle for correction versus zenith angle. Prism angle 0.5° off produces 3 mas residual atmospheric dispersion (shown the segment in I band).

degree order which encircled the dispersion within the AO corrected spot. Thus residual atmospheric dispersion value can be neglected (as it is within the diffraction limited spot width, ≈ 50 mas in $0.55 \mu\text{m}$) after correction by the atmospheric dispersion corrector, $\sigma_D^2 \approx 0$.

- **Low order tilt temporal error, σ_{TT}^2 :**

It depends on the atmospheric tip-tilt frequency and the correction frequency of the system; expressed as,

$$\sigma_{TT}^2 = \left(\frac{f_T}{f_{3DB}} \right)^2 \left(\frac{\lambda}{D} \right)^2 \quad (2.14)$$

where f_T and f_{3DB} are respectively the atmospheric tip-tilt frequency and the 3-DB servo bandwidth of the system for tip-tilt correction[3].

- **Low order tilt anisoplanatic error, σ_{TA}^2 :**

Low order tilt anisoplanatic error arises due to the distance of tip-tilt guide star from the target star and given below.

$$\sigma_{TA}^2 = \left(\frac{\theta}{\theta_{TA}} \right)^{\frac{5}{3}} \quad (2.15)$$

where θ is the angle of the tip-tilt star from the target star and θ_{TA} [3] is tilt isoplanetic angle given by,

$$\theta_{TA}^2 = \left[0.668k^2(\sec z)^3 \mu_2 D^{-1/3} \right]^{\frac{1}{2}} \quad (2.16)$$

where μ_2 is second order turbulence moment (Equation 3.21a of Hardy[3]).

TABLE 2.2: iRobo-AO Error Budget at Zenith under 1.2'' seeing condition (Hafnagel model).

| Source of errors | Wavelength | | | | |
|--|-----------------------|--------------|--------------|--------------|--------------|
| | 0.8 μm | 1.25 μm | 1.65 μm | 2.25 μm | 2.25 μm |
| Fried parameter, r_0 (m) | 0.1508 | 0.2554 | 0.3564 | 0.5170 | 0.5170 |
| Fitting Error, σ_{Fit} (rad ²)* | 0.4095 | 0.1703 | 0.0977 | 0.0525 | 0.0525 |
| Servo Lag Error (Temporal error/bandwidth), σ_{BT} (rad ²)* | 0.0067 | 0.0028 | 0.0016 | 0.0009 | 0.0009 |
| Beacon Measurement Error, σ_{BM} (rad ²)* | 0.4518 | 0.1879 | 0.1078 | 0.0580 | 0.0580 |
| Angular Anisoplanetic Error, σ_A (rad ²)* | 0.0286 | 0.0119 | 0.0068 | 0.0037 | 0.0037 |
| Focal Anisoplanetic Error/Cone effect σ_{FA} (rad ²)* | 4.0958 | 1.7029 | 0.9773 | 0.5256 | 0.5256 |
| Tilt Anisoplanetism σ_{TA} (rad ²)* | 0.7121 | 0.2961 | 0.1699 | 0.0914 | 0.0914 |
| Tilt temporal error σ_{TT} (rad ²)* | 0.0309 | 0.0128 | 0.0074 | 0.0040 | 0.0040 |
| Total Error, σ_{tot} (rad ²)* | 5.7354 | 2.3846 | 1.3686 | 0.7360 | 0.7360 |
| Uncorrected Strehl Ratio (%) | 0.5467 | 1.6500 | 3.2530 | 6.2197 | 6.2197 |
| Equivalent Corrected | | | | | |
| Strehl Ratio (SR) | 0.33 [‡] (I) | 9.50 (J) | 25.93 (H) | 45.40 (K) | 45.40 (K) |
| over the band (%)[†] | | | | | |

* Radians of phase

[†] Considering transmission profile of the filter.[‡] Uncorrected SR calculation is approximated which produces better than the AO corrected SR under high wavefront aberration.

TABLE 2.3: Expected AO-corrected Strehl Ratio.

| Seeing: 1.2'' at Wavelength(λ): 0.55 μ m, Zenith (z): 0 $^\circ$ | | | | | |
|--|------------------------|-------------|--------------|--------------|--------------|
| Band | $\lambda(\mu\text{m})$ | $z=0^\circ$ | $z=10^\circ$ | $z=20^\circ$ | $z=40^\circ$ |
| | | SR(%) | SR(%) | SR(%) | SR(%) |
| J | 1.25 | 9.50 | 9.11 | 7.97 | 3.89 |
| H | 1.65 | 25.93 | 25.34 | 23.39 | 15.23 |
| K | 2.25 | 45.40 | 44.75 | 42.72 | 33.19 |

One of the performance indicators of an AO system is measured by the Strehl ratio, and it is discussed here.

Strehl Ratio: The ratio of peak intensity in long exposure Point Spread Function (PSF) over that of the theoretical diffraction limited PSF [79] is called Strehl ratio and is given in Equation 2.17.

$$S = \frac{1 - \exp\left(\frac{\sigma^{-10/3}}{6}\right)}{1 + \left(\frac{D_{pupil}}{r_0}\right)^2} + \exp(\sigma^{-2}) \approx \exp(\sigma^{-2}) \quad (2.17)$$

where D_{pupil} , σ are the telescope diameter and rms wavefront error respectively. The expression of Strehl ratio for uncompensated atmosphere is given by,

$$S \approx \left(\frac{D_{pupil}}{r_0}\right)^{-2} \quad (2.18)$$

The effective Strehl Ratio over a band of a Filter is estimated by taking a weighted sum of Strehl ratios over the wavelength samples (transmission of the corresponding filter) followed by averaging given by,

$$S_{\text{effective over band}} = \frac{\sum S_{\lambda_i} \times \tau_{\lambda_i}}{\sum \tau_{\lambda_i}} \quad (2.19)$$

where τ_{λ_i} is the transmission of the filter at wavelength λ_i . We have calculated the expected effective Strehl ratio at different zenith angles and given in Table 2.3.

2.2 Description

A brief introduction of all the elements which are assembled in the Cassegrain AO facility are given here with specifications of the optics in Table 2.4.

TABLE 2.4: Specification of iRobo-AO Cassegrain Optics.

| Name of Optics | Specification |
|-----------------------|--|
| FM1(Elliptical) | Major and Minor Diameter: 35.3 mm and 20 mm, Thickness: 2 mm, Material: Fused Silica (UV grade) |
| OAP1 [†] | OAD [‡] : 23.556 mm, Parent ROC*: 78.056 mm, Material: Zerodur |
| DM (MEMS based) | Aperture: 4.4×4.4 mm ² , Continuous Surface Stroke: 3.5 μ m, Actuators: 140 |
| UV Arm Optics | |
| Laser Dichroic | Diameter: 22 mm, Thickness: 2 mm, Reflects 355 nm and Transmits 390 nm-2500 nm |
| Lens | Surface1, ROC: 141.669 mm (Convex), Surface2, ROC: 80.1968 mm (Convex), Center Thickness: 5mm, Diameter: 19 mm, Material: Fused Silica (UV grade) |
| FM4,5 | Diameter: 25.4 mm, Material: Fused Silica (UV grade) |
| OAP5 | OAD: 68.812 mm, Parent ROC: 303.086 mm, Material: Zerodur |
| Retarder | Retardation: $\lambda/2$ at 355 nm, Size: 10 × 10 × 1.6 mm ³ , Material: Quartz |
| Pockels Cell | BBO Pockel Cell at 355 nm, Aperture: 6 mm |
| SHWFS | Plano-convex, Focal length: 76.6 mm @633 nm, Lenses Array: 11 × 11, Each lenslet size: 0.5 × 0.5 × 1 mm ³ |
| Analyzer | Polarizing cube beam-splitter, 15 × 15 × 15 mm ³ , Material: Fused Silica (UV grade) |
| Relay lens1 | Surface1, Plane, Surface2, ROC: 38.6 mm (Convex), Center Thickness: 2 mm, Diameter: 15 mm, Material: Fused Silica (UV grade) |
| Relay lens2 | Surface1,2 ROC: ± 21.5 mm (Convex), Center Thickness: 3.1 mm, Material: Fused Silica (UV grade), Diameter: 15 mm |
| CCD39 | e2v CCD39 chip, 80×80 pixels each of size 24 μ m |

Continued on next page

Table 2.4 – continued from previous page

| Name of Optics | Specification |
|-----------------------------------|--|
| | Plate scale: 0.675"/pixel |
| Visible and IR Arms Optics | |
| OAP2 | OAD: 62.648 mm, Parent ROC: 118.919 mm, Material: Zerodur |
| OAP3 | OAD: 57.595 mm, Parent ROC: 326.64 mm, Material: Zerodur |
| OAP4 | OAD: 304.468 mm, Parent ROC: 730.583 mm, Material: Zerodur |
| FM2,TTM | Diameter: 30 mm, Material: Zerodur |
| ADC | IGO specific design (Fig. 4.4) |
| Science Dichroic | Diameter: 76 mm, Thickness: 10 mm, Reflects visible (390 nm-900 nm) and Transmits NIR Spectrum(900 nm-2500 nm) |
| FM3 | Diameter: 101.6 mm, Thickness: 19.1 mm, Material: Fused Silica, Coating: Protected Gold (700-10000 nm) |
| Visible Filters | Bessell U, B, V, R and I, Diameter: 25 mm, Thickness: 5 mm |
| EMCCD | 1K×1K (Andor iXon3 888 chip) with 13 μm pixel size, Plate scale: 2.25"/mm |
| †OAP: Off axis parabolic mirror | |
| ‡OAD: Off axis distance | |
| *ROC: Radius of Curvature | |

iRobo-AO uses a total of five custom made Off-Axis Parabolic Mirrors (OAP) mirrors to relay light from the telescope focus to the various components of the visible, IR and UV arms. They also help in reimaging the telescope entrance pupil on the DM, ADC and the wavefront sensor.

We have seen from section 2.1.1.4 that the prescriptions for the Deformable Mirror (DM) are 12×12 actuators array with $\approx 1.5 \mu\text{m}$ stroke for separate tip-tilt correction. The Boston Micromachine MEMS based DM with a maximum stroke

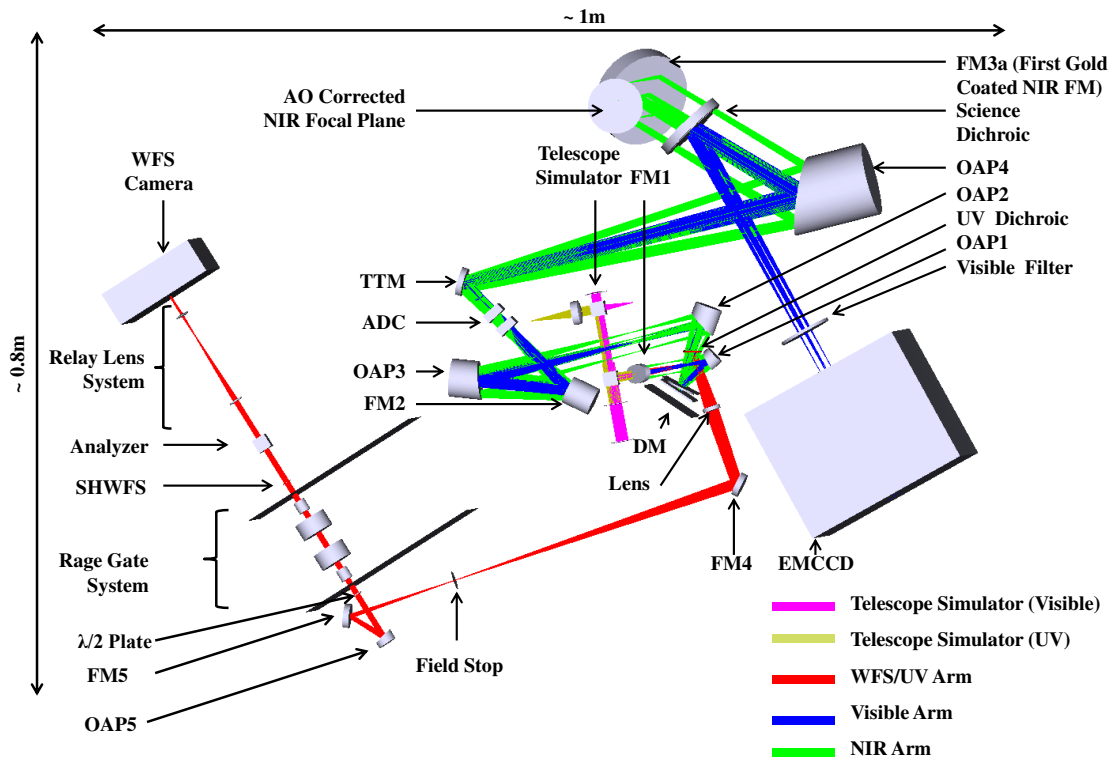


FIGURE 2.4: iRobo-AO optical layout.



FIGURE 2.5: Mechanical design, the orientation of the layout is identical to that of the optical layout Fig.2.4.

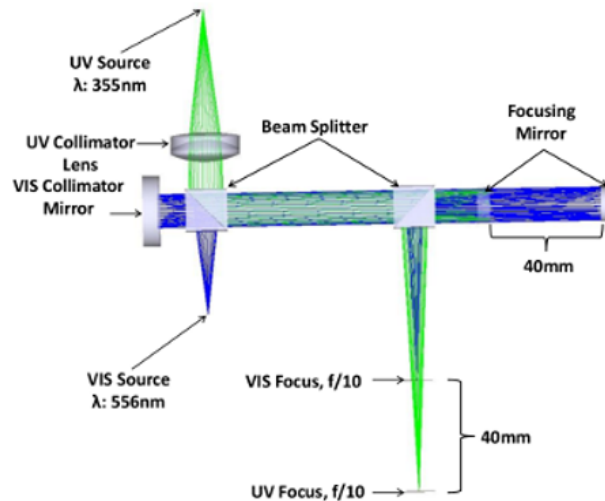


FIGURE 2.6: Optical layout of telescope simulator.

size of $3.5 \mu\text{m}$, clear aperture of 4.4 mm and a total of 140 working actuators was selected for iRobo-AO to handle the higher order corrections only. The entrance pupil of the telescope can be first re-imaged on the DM surface across its clear working aperture of 4.4 mm.

A set of two dichroic filters are used to split the input beam into the UV, visible and IR arms, - more details are given in optical relay paragraph.

Two motorized filter wheels each with six slots are mounted in front of the EMCCD science camera. A set of Bessell U, B, V, R and I filters are mounted in the slots. The rest of the slots will be populated as per future requirements.

The atmospheric dispersion also imparts serious effects especially when observing objects at large zenith angles. In such cases the images of the objects generally tend to elongate due to dispersion. The Atmospheric Dispersion Corrector (ADC) is discussed at length in chapter 4.

We have seen in section 2.1.1.5 that the required dynamic range for the platform of the tip-tilt mirror is ≈ 1 mradian. Hence the chosen piezo tip-tilt platform³ with a maximum stroke of 2 mradian is sufficient for our purpose. Both the ADC and TTM are common to the visible and IR arm. It needs to be mentioned here that although a TTM is an integral part of iRobo-AO, it can be used to its full capacity only after the NIR camera is commissioned. Either the EMCCD visible

³Physic Instrument S-330.20L tip-tilt stage have maximum 3.5 mrad tilt capability in both axis.

camera or the NIR camera can be used for tip-tilt correction depending on the science arm we choose. It is controlled by detecting the motion of the center of the gravity of fast read-out images by either visible or NIR camera. Alternatively, Lucky imaging technique [18, 80] can be used for tip-tilt removal.

iRobo-AO uses a $1K \times 1K$ EMCCD (Andor iXon3 888) with $13 \mu\text{m}$ pixel size as the science camera in the visible arm ($0.4\text{-}0.9 \mu\text{m}$). The camera can function both in single and in rapid frame modes with different predefined EM gain. There are a total of 16 preset modes in which the camera can operate and this also includes tip-tilt mode. The fast readout of the camera (~ 9 full frames per sec.) enables tip-tilt correction even without the NIR camera. The data are stored in fits cube format and is processed with a shift and add Lucky imaging algorithm [18, 80]. The plate scale and the FOV are $2.25''/\text{mm}$ and $\pm 15''$.

The beam from the laser projector is continuously Rayleigh scattered as it propagates upwards through the atmosphere. To pickup the scattered light only from within the Rayleigh depth and to stop the stray scattered light from reaching the wavefront sensor a range gating system [81] is installed. The gating works by opening a high speed electro-optical shutter based on Pockels effect for a specific time such that only the scattered light from the Rayleigh depth reaches the wavefront sensor. More details are given in section 2.3.5.4. The gating system is coupled with a delay generator to account for the return time of the pulse and can be individually programmed for delay and pulse width adjustments.

iRobo-AO uses a Shack Hartmann lenslet array for a Wavefront Sensor which is made of a rectangular array of 11×11 plano-convex lenslets⁴, each of focal length 76.6 mm , and pitch 0.5 mm . It is placed immediately after the Pockels cell. The wavefront sensing camera has a e2v CCD39 chip, which has 80×80 pixels each of size $24 \mu\text{m}$. There are four amplifiers at four corners of the CCD39 which can be read simultaneously for fast readout. More details on the wavefront sensing structure of the CCD39 camera are presented in section 2.9. The plate scale and the FOV/subaperture are $0.675''/\text{pixel}$ and $4''$.

An internal telescope optics simulator (the magenta and yellow path in Fig. 2.4) is also an integral part of iRobo-AO. The entire optical alignment of iRobo-AO has been done using the simulator. It has the capability to simulate two foci -one

⁴Advanced Microoptic Systems GMBH 15×15 microlens array was purchased and only central 11×11 array are used.

for a UV source at a finite height of say 10 km above the telescope and second for a source at infinity in the visible band. In both case, the f/number is matched with that of the telescope beam. A fold mirror (FM1) mounted on a linear stage is used to direct the light from the telescope into the main AO system. Fig. 2.6 shows the optical layout of telescope simulator, it can be seen that the UV (LGS) focus and the visible (target) focus are separated by 40 mm with f/10 beam as in the case with telescope optics.

Optical Relay As shown in Fig.2.4 the incoming light from the telescope is first directed perpendicular to the telescope axis with the help of a fold mirror (FM1) and the telescope entrance pupil is first re-imaged on the DM with OAP1. After reflection from the DM and with the help of a dichroic filter (UV dichroic) all the UV light is reflected towards the wavefront sensing arm. The transmitted visible and NIR beam after reflection from OAP2 and OAP3 passes through the ADC and is guided by the TTM to OAP4. Finally with the help of another dichroic filter (science dichroic) the visible light is passed to the EMCCD and the NIR light to the NIR camera.

In the UV arm, with the help of a lens and OAP5 the pupil is again re-imaged on the SHWFS after passing through the range gating system. The range gating system is mounted between two crossed polarizing beam splitters (PBS). A rotating half wave plate retarder at the entrance of the first PBS keeps the polarization axis of the LGS light fixed with respect to the axis of the polarization components following it. The range gating system is discussed in detail in section 2.3.5.4. Finally the image after the SHWFS is relayed to the CCD39 with a pair of relay lenses. Fig. 2.4 shows the complete optical relay and the complete mechanical modelling of iRobo-AO Cassegrain AO facility is shown in Fig. 2.5.

2.3 Optical Alignment

The assembly and integration of the optics and its validation is described in this section. Inspections and testings of all individual hardware components of iRobo-AO, like DM, TTM, FSM, Pockel Cell, Delay Generator, Andor EMCCD camera, CCD39 wavefront sensing camera, OAPs, Filter Wheels, etc. are done before starting the optical alignment process.

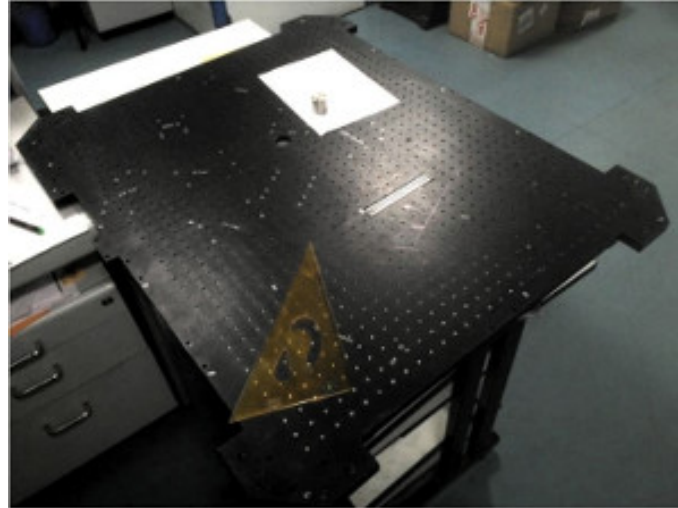


FIGURE 2.7: Breadboard of Cassegrain box (AO facility): the optical layout has been marked.

The integration and development process and tests are described here sequentially following the light path.

2.3.1 Breadboard(BB) Drawing

Optical integration starts with the breadboard/ base plate of the Cassegrain AO box (facility). The breadboard is adequately cleaned and checked, such that no burrs are trapped in any of the tapped holes. This step avoids unwanted scratches on any optics due to the burrs when the Cassegrain AO box is mounted in the telescope in upside down orientation. As per the mechanical and optical design of the system, the optical layout first sketched on the breadboard (Fig. 2.7). The drawing helped to place the components roughly at the right location at the time of the optical alignment.

2.3.2 Elliptical Fold Mirror

Once the telescope $f/10$ beam enters the instrument (Cassegrain box), it is reflected by 90° by the elliptical plane mirror (FM1) towards the first off-axis parabolic mirror OAP1 and places the telescope focus at the right location in front of the OAP1. Thus OAP1 produces image of pupil at the center of deformable mirror. The elliptical mirror is mounted on a two-axis tip-tilt adjustable optomechanical

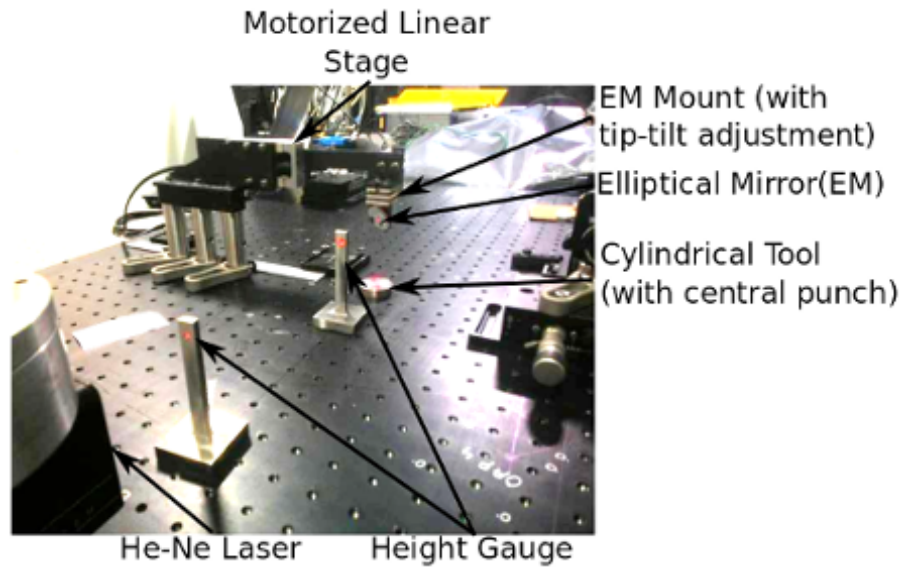


FIGURE 2.8: Elliptical fold mirror.

mount for on sky alignment of the image of the telescope pupil with the deformable mirror. The entire unit (elliptical mirror + two-axis tip-tilt adjustable mount) is mounted on a motorized linear stage to switch between on-sky light and laboratory telescope simulator light.

The central point of the mirror is kept vertically above the centre of the light entering the aperture of the breadboard at a height of 75.891 mm as per the Zemax design. This alignment is done using a metal cylinder with a central punch (called cylindrical tool, mentioned in the setup Fig. 2.8) placed at the breadboard aperture (without any play in the aperture), and a He-Ne laser beam employing a back reflection technique and beam height measurement gauge. The He-Ne laser beam (made horizontal to breadboard at the height of ~ 75.9 mm.) is launched from the OAP1 position and incident at the aperture centre of the elliptical mirror. The mirror is adjusted so that the reflected light hits the centre punch of the cylinder (Fig. 2.8). A mirror was kept on the cylindrical tool (parallel to the breadboard surface) to let the light reflect back to the laser aperture. It is to be also ensured that the elliptical mirror assembly should not block the light in the science arm or hit any other components during the motion of the linear motorized actuator as the area around it is very crowded with, DM, Laser dichroic, OAP1, FM2 etc.

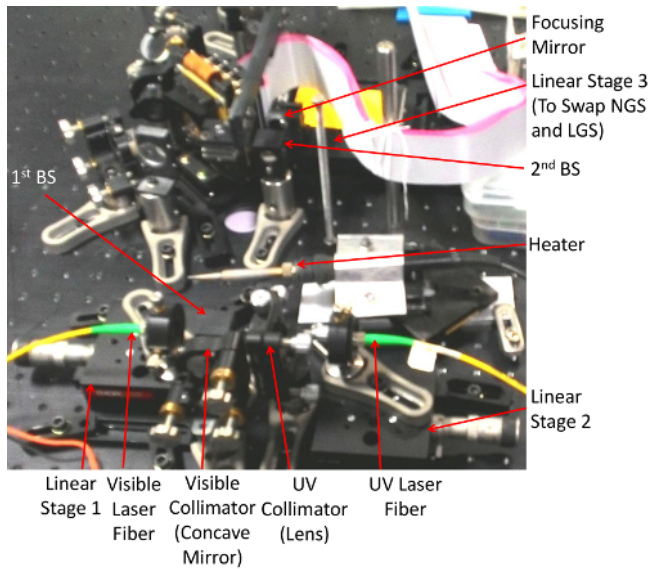


FIGURE 2.9: Telescope simulator.



FIGURE 2.10: Shearing interferometer.

2.3.3 Telescope Simulator

The telescope simulator is critical in the laboratory optical alignment process. It does not mimic the secondary obscuration but produces an $f/10$ beam which is identical to that of the telescope, using an aperture. We have two laser sources visible (green: $0.556 \mu m$) for science and UV ($0.355 \mu m$) for UV/WFS arm alignment respectively. These are fiber coupled with FC-APC connectors in the telescope simulator. The UV and green fiber tips are kept at the back focal plane of a UV biconvex lens and a concave mirror respectively to produce corresponding collimated beams (Fig. 2.9). The quality of the collimation is checked with a shearing interferometer (Fig. 2.10) as given below.

Shearing Interferometer: The lateral shearing interferometer[82] introduces shear orthonormal to the tilt direction. A wavefront with only defocus is represented in Eqn. 2.20, where D is the coefficient of defocus.

$$W(x, y) = D(x^2 + y^2) \quad (2.20)$$

A wavefront with only primary spherical aberration is represented in Eqn. 2.21, where A is the coefficient of spherical aberration.

$$W(x, y) = A(x^2 + y^2)^2 \quad (2.21)$$

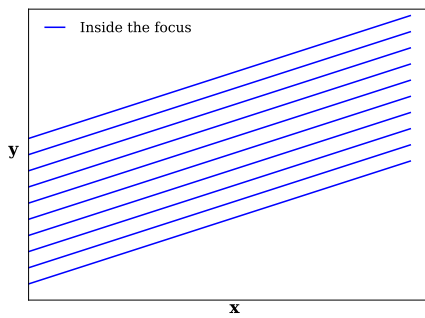


FIGURE 2.11: Interferogram: inside the focus (defocus term, $D=1$; tilt term, $E=5$ and shift term, $S=1$).

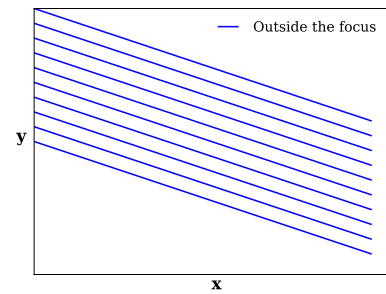


FIGURE 2.12: Interferogram: outside the focus (defocus term, $D=-1$; tilt term, $E=5$ and shift term, $S=1$).

Let ‘S’ amount of lateral shift in the x-direction and tilt with coefficient E in the y-direction are given by the shearing interferometer (both wavefronts intersect along the x-axis). The value of E is shearing interferometer dependent. Interferometer generates two wavefronts due to reflections from the front and back surfaces of the glass plate. The back reflection introduces shear and tilt about the first reflected wavefront.

The optical path difference between the two sheared wavefronts with defocus term is given by,

$$\Delta W(x, y) = (2Dx + Ey)S \quad (2.22)$$

If there is primary spherical aberration and defocus then the optical path difference becomes

$$\Delta W(x, y) = \{4A(x^2 + y^2)x + 2Dx + Ey\}S \quad (2.23)$$

Using Eq. 2.22 three plots are made to understand how fringes rotate as the defocus term goes negative to positive angle with $S=1$. Fig. 2.11 depicts the fringes when $D=1$ and $E=5$, inside the focus. Fig. 2.12 describes the fringes when $D=-1$, and $E=5$, outside the focus. Fig. 2.13 represents the fringes when $D=0$ at the focus and $E=5$. The fringe pattern with spherical aberration is visualised plotting Eqn. 2.23. The fringes with $D=-1$ outside the focus, $A=-0.1$ primary spherical aberration and $E=5$ looks like ‘S’(Fig. 2.14).

The fiber mount of the telescope simulator is mounted on a linear translational stage such that the laser fiber tip can be moved back and forth for achieving collimation. The beam is collimated using the shearing interferometer. Straight

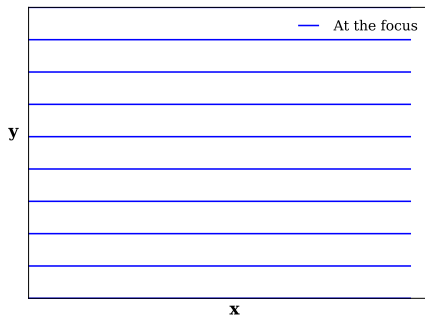


FIGURE 2.13: Interferogram: At focus (defocus term, $D=0$; tilt term, $E=5$ and shift term, $S=1$).

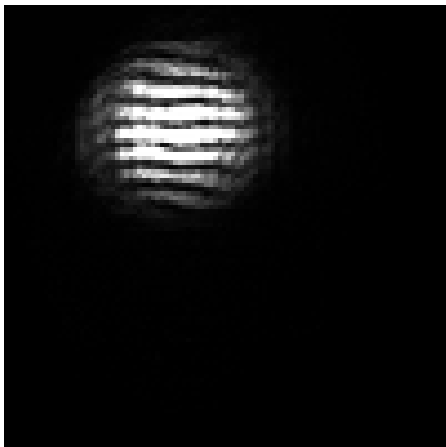


FIGURE 2.15: Visible collimation interferogram.

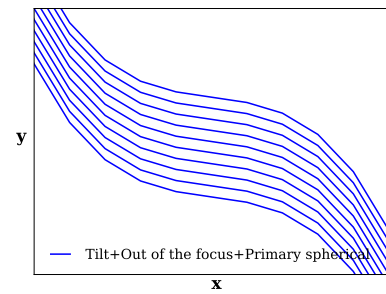


FIGURE 2.14: Interferogram: outside the focus+primary spherical (defocus term, $D=-1$; tilt term, $E=5$; shift term, $S=1$ and spherical aberration term $A=-0.1$).

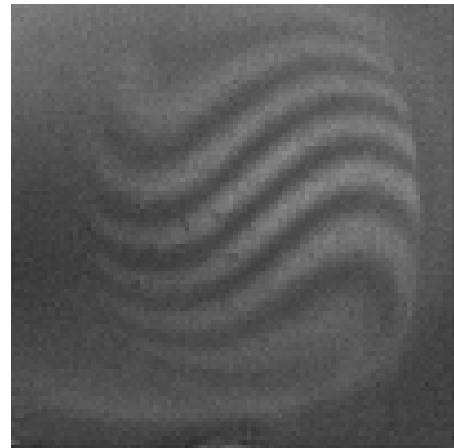


FIGURE 2.16: UV collimation interferogram (re-imaged on ST9 hence size changed w.r.t. Fig. 2.15).

line fringes of the interferogram (Fig. 2.15) along the shift in the visible arm of the telescope simulator proves the collimation of the beam without any significant aberration in the wavefront; similar to Fig. 2.13. On the other hand, there are ‘S’ type fringes in the interferogram of UV collimated beam (Fig. 2.16) with a minimum number of fringes.

This indicates that the beam is collimated but has primary spherical aberration (Fig. 2.14), probably due to the UV biconvex lens that has been used.

A pair of beam splitters are employed to reflect the beam without any obscuration towards the telescope focus. There is a concave mirror to focus the collimated

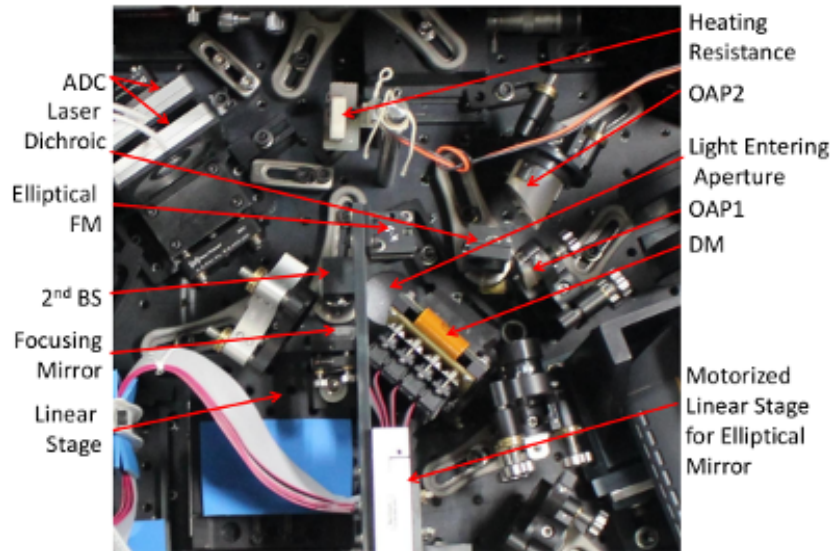


FIGURE 2.17: Aperture on the breadboard with components marked.

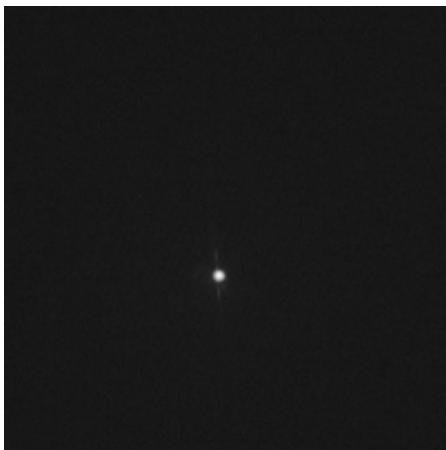


FIGURE 2.18: Visible spot of telescope simulator at telescope focus.

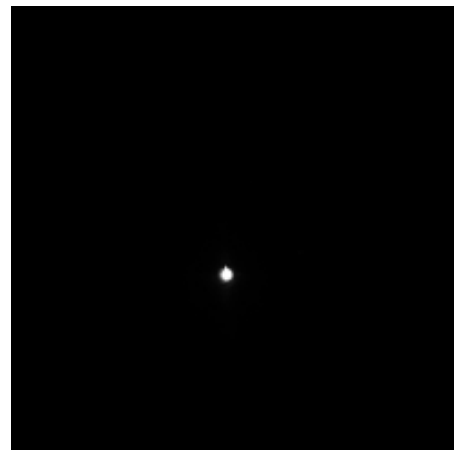


FIGURE 2.19: UV spot of telescope simulator at telescope focus.

beam to form an $f/10$ beam which is identical to the telescope f -number. The visible and UV spots are given in Figs. 2.18 and 2.19 respectively taken by SBIG ST9 camera of square $20 \mu\text{m}$ pixel. The separation between the two foci is $\approx 152.31 \mu\text{m}$ which corresponds to $1.564''$ in sky⁵.

It is to be kept in mind that the LGS is at a finite height (~ 10 km) and telescope forms image of LGS 40 mm away from the telescope focus. In the simulator this is achieved by moving the said focusing mirror (concave) by 40 mm. The mirror

⁵Plate scale at the telescope focus is $10.3''/\text{mm}$

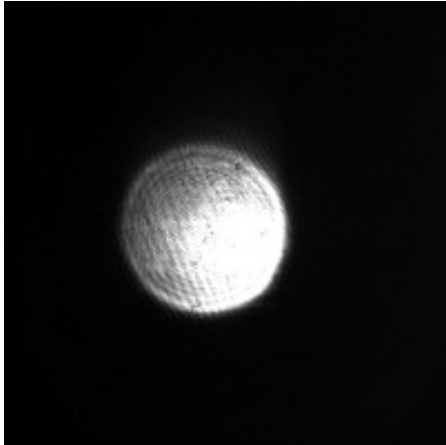


FIGURE 2.20: Cross-section of UV collimated beam by OAP1.

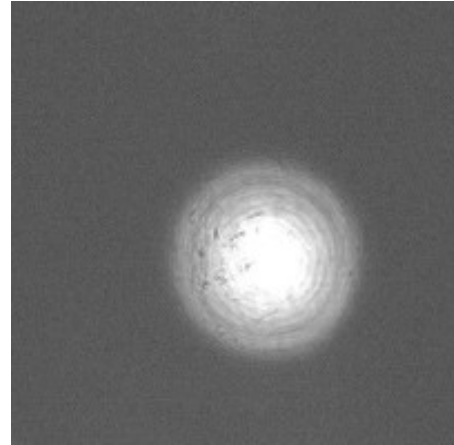


FIGURE 2.21: Cross-section of visible collimated beam by OAP1.

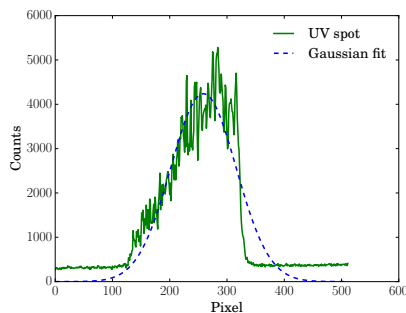


FIGURE 2.22: UV collimated beam profile.

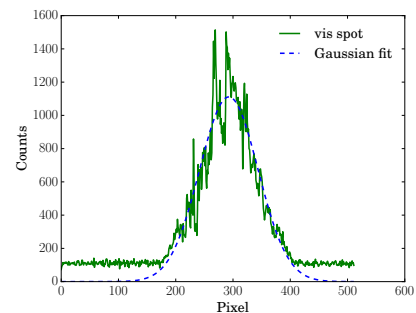


FIGURE 2.23: Vis. collimated beam profile.

is mounted on a linear stage with sufficient dynamic range to switch between LGS and natural mode.

2.3.4 Common elements of UV, Visible and IR Arm

2.3.4.1 OAP1

OAP1 is the second optical component of the AO system after the elliptical mirror. It collimates the telescope $f/10$ beam and makes a pupil at the Deformable Mirror. The collimated beams in both UV and visible are given in Fig. 2.20⁶ and 2.21. There are several stray straight line fringes due to ghost reflections as well as a diffraction pattern produced by a circular aperture in both Figures. A row of pixels along the center of the both the UV and visible spots (Fig. 2.20 and 2.21) are

⁶to align OAP1, UV focus is also kept at the telescope focus identical to the visible source.

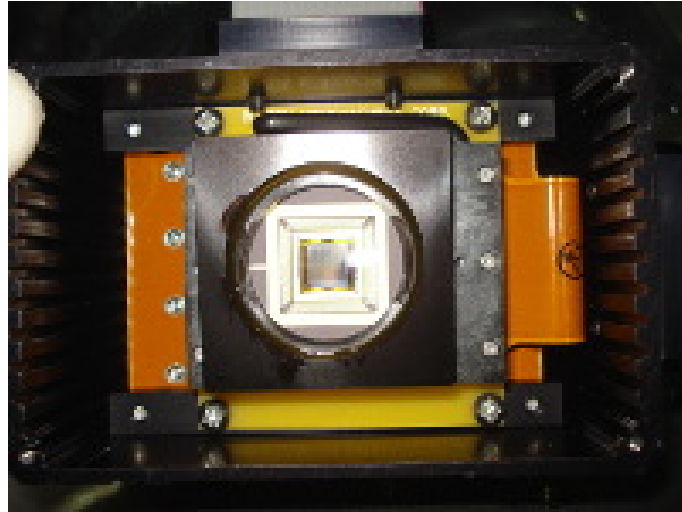


FIGURE 2.24: DM with external safety covers.

| | | | | | | | | | | | |
|-----|-----|-----|-----|-----|-----|-----|-----|-----|-----|-----|-----|
| | 1 | 2 | 3 | 4 | 5 | 6 | 7 | 8 | 9 | 10 | |
| 11 | 12 | 13 | 14 | 15 | 16 | 17 | 18 | 19 | 20 | 21 | 22 |
| 23 | 24 | 25 | 26 | 27 | 28 | 29 | 30 | 31 | 32 | 33 | 34 |
| 35 | 36 | 37 | 38 | 39 | 40 | 41 | 42 | 43 | 44 | 45 | 46 |
| 47 | 48 | 49 | 50 | 51 | 52 | 53 | 54 | 55 | 56 | 57 | 58 |
| 59 | 60 | 61 | 62 | 63 | 64 | 65 | 66 | 67 | 68 | 69 | 70 |
| 71 | 72 | 73 | 74 | 75 | 76 | 77 | 78 | 79 | 80 | 81 | 82 |
| 83 | 84 | 85 | 86 | 87 | 88 | 89 | 90 | 91 | 92 | 93 | 94 |
| 95 | 96 | 97 | 98 | 99 | 100 | 101 | 102 | 103 | 104 | 105 | 106 |
| 107 | 108 | 109 | 110 | 111 | 112 | 113 | 114 | 115 | 116 | 117 | 118 |
| 119 | 120 | 121 | 122 | 123 | 124 | 125 | 126 | 127 | 128 | 129 | 130 |
| | 131 | 132 | 133 | 134 | 135 | 136 | 137 | 138 | 139 | 140 | |

FIGURE 2.25: DM active actuators (highlighted).

plotted in Fig. 2.22 and 2.23. It can be noticed that there is a shift of the center of the circular boundary from the peak value of UV spot (Fig. 2.22) because of vignetting somewhere in telescope simulator UV path. It also introduces a gradual change of the intensity in Fig. 2.20. But the visible spot peak intensity coincides with the center of the spot (Fig. 2.23) as there is no vignetting. Both collimations were examined with the shearing interferometer.

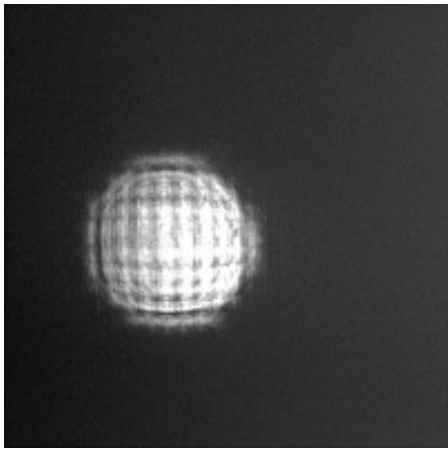


FIGURE 2.26: Reflected UV collimated light from DM under flat condition.

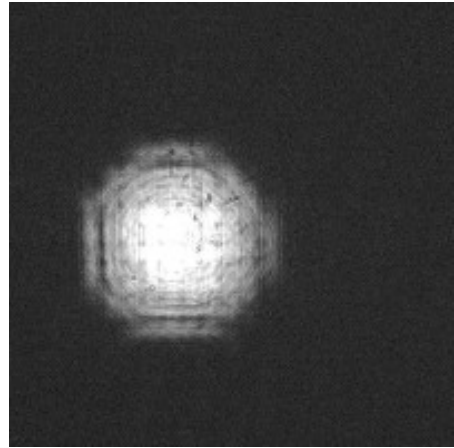


FIGURE 2.27: Reflected visible collimated light from DM under flat condition.

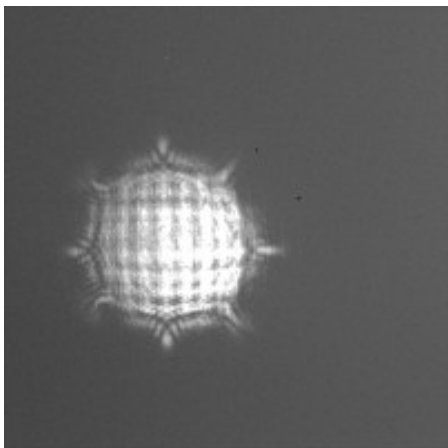


FIGURE 2.28: Reflected UV collimated light beam from the DM when peripheral 8 actuators are poked by an identical amount, the impression of the poke to all actuators are equal to all.

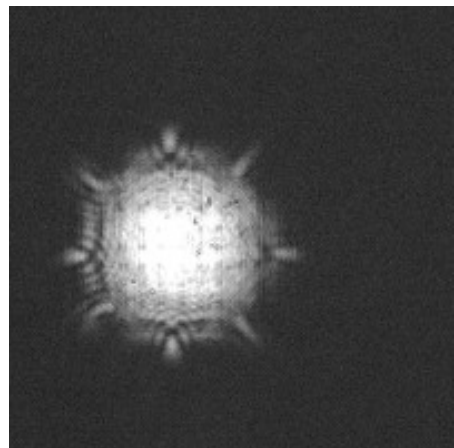


FIGURE 2.29: Reflected visible collimated light beam from the DM when peripheral 8 actuators are poked by an identical amount, the impression of the poke to all actuators are equal to all.

2.3.4.2 Deformable Mirror (DM)

The size of the DM with its external protective cover (Fig. 2.24) is large compared to the available space around it. The protective external cover is removed and DM is attached to a bracket and mounted on a four-axis (X, Y, θ_x , θ_y) tilt aligner mount. There are a total of 120 active actuators (Fig. 2.25) out of total 140 that are within the illuminated pupil and used in the wavefront reconstruction. The illuminated pupil contains only 97 subapertures. The pupil size in visible ($\lambda : 0.556\mu\text{m}$) as well as in UV ($\lambda : 0.355\mu\text{m}$) is 4.4 mm. Both reflected beam in UV and visible light from DM (Fig. 2.26 and 2.27) shows that the beam is completely within the DM active area as per prescription without any vignetting from the DM surface. It is verified that all the active actuators (Fig. 2.25) are within the light beam at the DM by poking all the peripheral actuators (total eight actuators [5, 33, 59, 117, 135, 108, 70, 24]) and checking their appearance in both the spots (Figs. 2.28 and 2.29).

2.3.5 UV Arm

The UV arm contains a Laser dichroic mirror, a lens (aspheric), two fold mirrors (FM4 and FM5), a field stop, OAP5, half wave plate (HWP), range gate system, SHWFS, relay lens system and CCD39.

2.3.5.1 Laser Dichroic

The DM reflects the entire wavelength range, UV to IR. The LGS emits 355 nm laser line light. A dichroic mirror is placed after DM, which reflects the 355 nm light and steers it to the WFS arm. Laser dichroic transmits the rest of the spectrum for the visible and NIR arms. Astigmatism⁷ was initially noticed in the beam coming off the laser dichroic. This was traced as due to stress introduced in the 2 mm thin dichroic by the custom made optomechanical mount.

⁷Astigmatism is the power difference between the Sagittal and Tangential plane (Fig. 2.31). It is the third term of the Seidel aberration. It is represented by $b_3 y^2 \eta^2$, where b_3 , y and η are respectively the coefficients of astigmatism, the Cartesian coordinate at the pupil and the Cartesian coordinate at image plane [83].

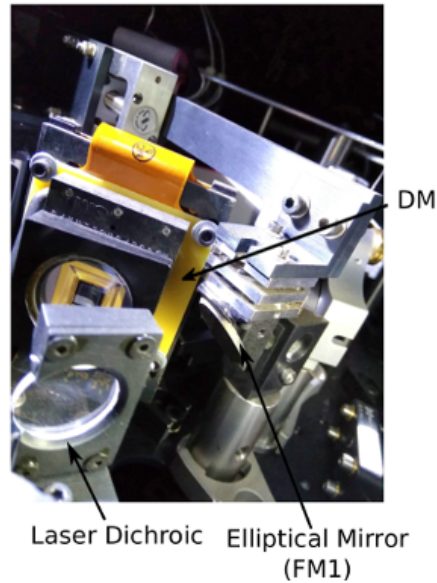


FIGURE 2.30: Laser dichroic assembly.

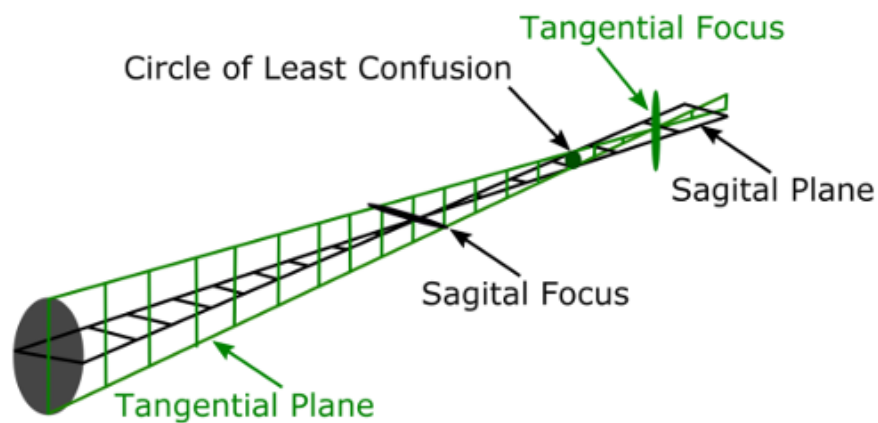


FIGURE 2.31: Schematic diagram of astigmatism.

2.3.5.2 Lens (Aspheric)

The position of the image of the UV fiber tip / LGS produced by the aspheric lens (before the OAP5) is very sensitive to the location of the aspheric lens because the LGS focus (adjacent to the OAP1) is very close to the back focal plane of the aspheric lens ($f < \text{object distance of aspheric lens (LGS)} < 2f$). This leads to noncollimation as well as variation in the location of the pupil produced by OAP5. The pupil diameter at the SHWFS is 5.5 mm to cover the 11×11 lenslet array for the prescribed pupil sampling. Thus the location of the aspheric lens is

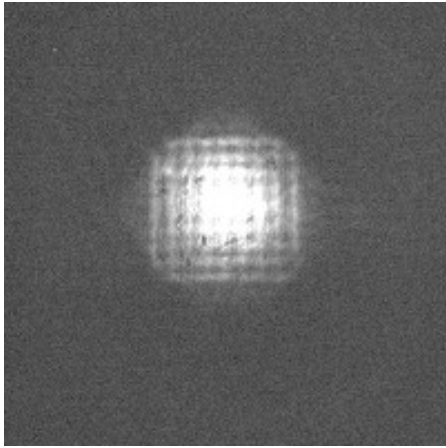


FIGURE 2.32: At some distance after aspheric lens in visible light under flat DM.

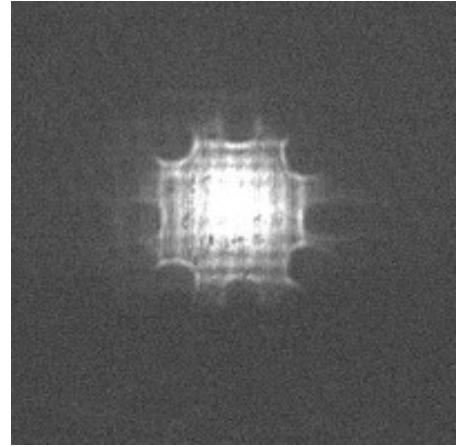


FIGURE 2.33: At some distance after aspheric lens in visible light when the peripheral actuators are poked.

very crucial in this regard and a number of iterations were needed to achieve the correct position. Another requirement is to check for any cutting or vignetting of the light due to the aspheric lens. Fig. 2.32 and 2.33 are taken when the DM is flat (flat map is loaded) and by poking all the peripheral actuators of the pupil. All the peripheral actuators are visible, which signifies that there is no vignetting by the aspheric lens. Fig. 2.33 looks different from Fig. 2.29 which is taken just after DM. It is like the same feature from the opposite direction. The wavefront after DM is flat but just after aspheric lens it is spherical and converging. Hence the difference is observed.

2.3.5.3 OAP5

The OAP5 collimates the diverging UV beam produced by the aspheric lens and forms a pupil at the SHWFS plane. The collimation is obtained through the best interferogram (Fig. 2.34) at the shearing interferometer with the DM in flat condition. The wavefront has little defocus term as discussed in Shearing Interferometer section 2.3.3. The pupil location is identified by observing the sharp features of the DM surface texture and is evident in Fig. 2.35 at the SHWFS plane.

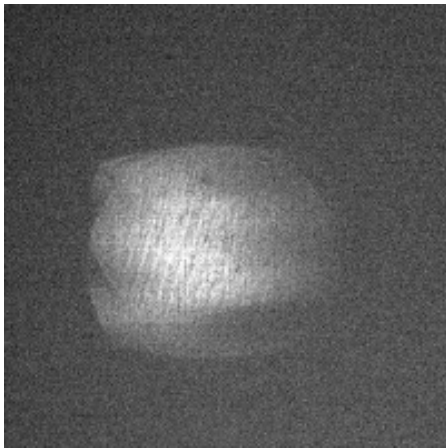


FIGURE 2.34: UV collimation (shearing interferometer o/p).

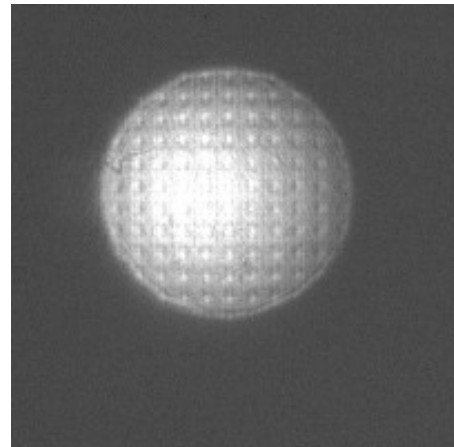


FIGURE 2.35: UV pupil at SHWFS.

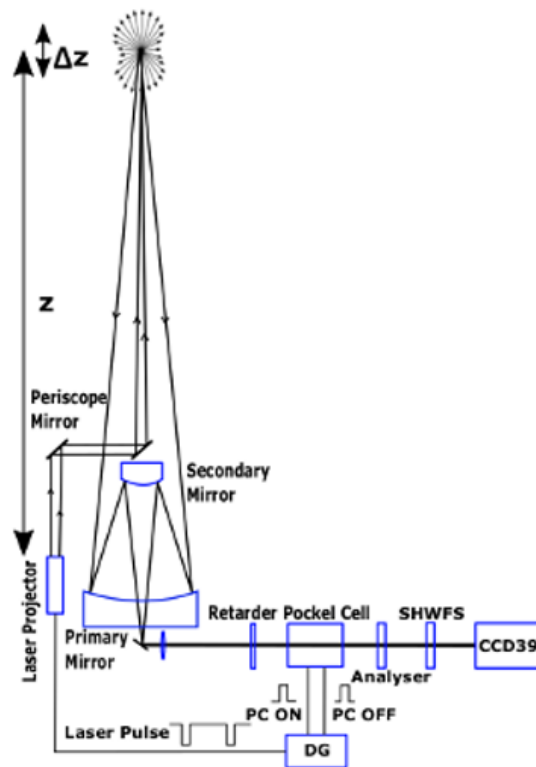


FIGURE 2.36: Schematic diagram of Range Gate.

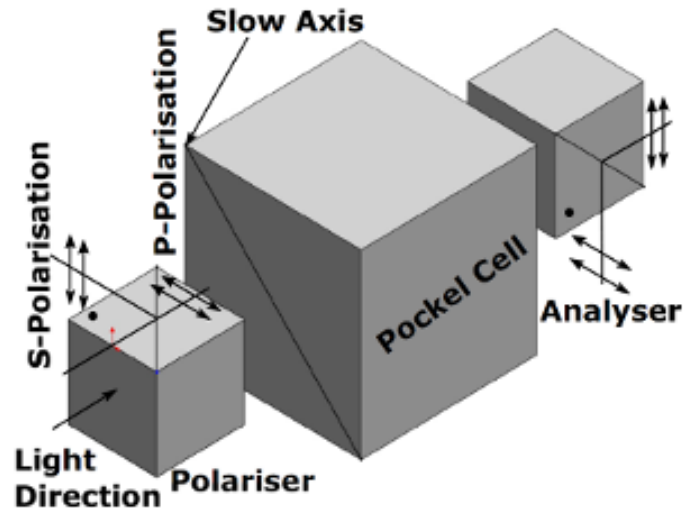


FIGURE 2.37: RG shutter action.

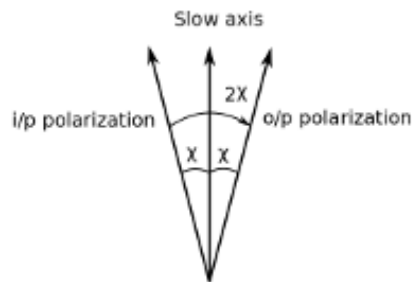


FIGURE 2.38: HWP's rotation of polarization action.

2.3.5.4 Range Gate (RG)

At the heart of the LGS based AO system is a 10 Watt Q-switched UV pulse laser of pulse width 33 ns and 10 kHz repetition rate. A switched signal from the laser that is synchronized with the laser light pulse is fed to the delay generator (DG), which triggers the on-off states of the Pockels cell electro-optical shutter (Fig. 2.36). When the appropriate voltage is applied to the Pockels cell (PC), it behaves like a half wave retarder⁸ in the optical path. The Pockels cell is

⁸Retarder-Half Wave Plate: The Retarder introduces 180° phase shift ($\lambda/2$ OPD) to the electric field of the fast-axis component to the input polarized light. It is called Half-Wave Plate (HWP) as it introduces $\lambda/2$ OPD. Let χ be the angle between the slow axis of the retarder and electric field of the input light. It rotates the plane of polarization of light passing through it by 2χ towards the slow axis [84]. Always it is required to align the retarder with the Pockel Cell such that the o/p polarization of it (Fig.2.38) along the horizon/breadboard plane surface. The input polarization always changes due to Cassegrain derotator. A HWP is mounted in front of the Range Gate on a motorized rotating stage to bring back the polarization along the parallel plane of the breadboard surface.

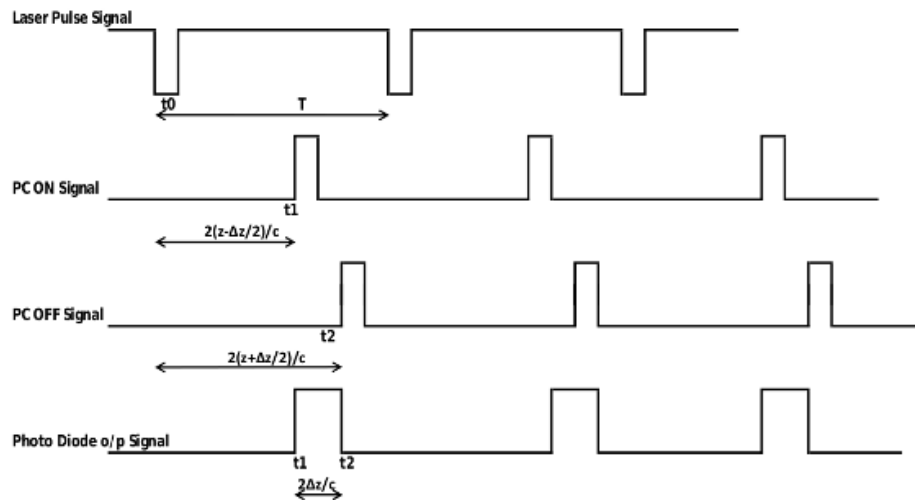


FIGURE 2.39: Timing diagram of the RG system.

FIGURE 2.40: Laser pulse, yellow line: square unit is $20\ \mu\text{sec}$, time period: $100\ \mu\text{sec}$, pulse repetition: 10 kHz.

placed between two orthogonal polarizing beam splitters (PBS)(Fig. 2.37). When a voltage as high as 3.3 kV (for 355 nm) is applied to the Pockels cell the shutter switches to ‘open’ mode and the beta- BaB_2O_4 crystal of the Pockels cell rotates the plane of polarization of the input beam by 90° which can pass through the orthogonal PBS. When no voltage is applied to the crystal the light is blocked by the crossed PBS.

The entire shuttering action for the range gate is explained here with the timing diagram (Fig. 2.39) and time delay estimation.

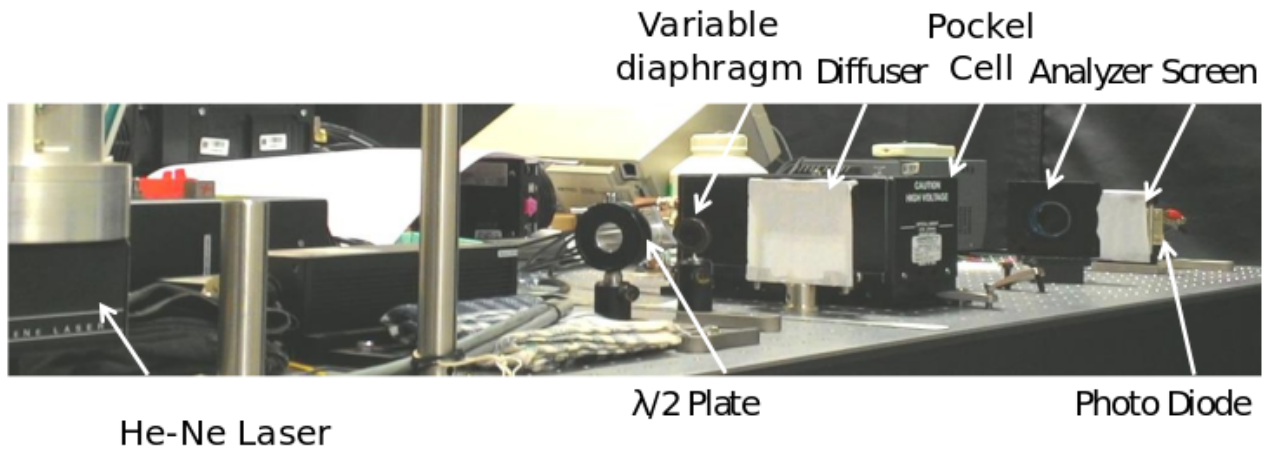


FIGURE 2.41: Experimental setup for Pockel Cell alignment and range gate shutter action.

The time taken by the laser pulse to travel from laser head to Pockel cell (PC) due to Rayleigh scattering from the lower and upper end of the Rayleigh depth are given by,

$$\begin{aligned}
 t_1 &= 2 \frac{(z - \Delta z/2)}{c} \\
 t_2 &= 2 \frac{(z + \Delta z/2)}{c}
 \end{aligned}
 \tag{2.24}$$

where Δz is the Rayleigh depth and c is the speed of light. Thus the required shutter open time to receive all the photons from the said Rayleigh depth is

$$\Delta t = t_1 - t_2 = \frac{2\Delta z}{c}.
 \tag{2.25}$$

It can be noticed that in the timing diagram, Fig. 2.39 the Delay Generator (DG) sends shutter ON and OFF signal to Pockel Cell for shuttering action at times t_1 and t_2 after ejection of a laser pulse. The actual laser signal is given in Fig. 2.40, which is a negative pulse. The falling edge conveys the starting time of the laser light pulse. Thus the negative edge trigger is used at the Delay Generator. It is to be remembered that the laser signal pulse width is different from the laser light pulse width (33 ns). The details of the laser guide star are given in the next Chapter 3.

An experimental setup (Fig. 2.41) was made to test the RG shutter action in the laboratory. A commercial laser (He-Ne, polarized at 45°) is first made parallel

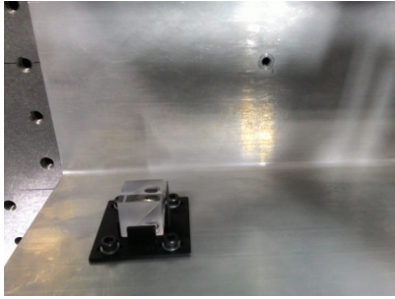


FIGURE 2.42: Polarizer at the side of the Pockel Cell, with in the cover.



FIGURE 2.43: Pockel cell is mounted on gimbal mount.

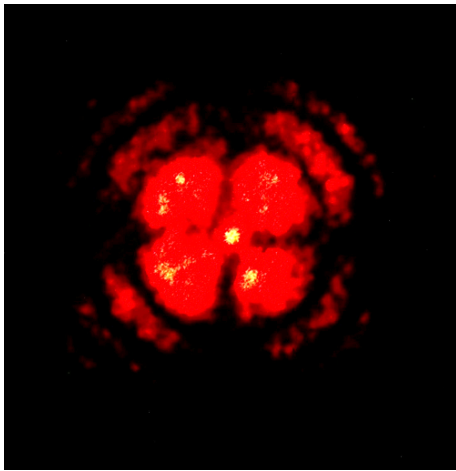


FIGURE 2.44: Isogyres as seen on a screen.



FIGURE 2.45: Delay Generator: active low triggering mode.

to the optical bench. Pockel Cell (PC) shutter is carefully inserted in the optical path on the optical bench to ensure that the laser beam transit the crystal parallel to the direction of the crystal's Z axis. A half wave plate is used after the laser to make the polarization on He-Ne laser vertical in the setup. A variable diaphragm is used to get a narrow pencil of the laser beam. A diffuser is kept in front of the Pockel Cell to make the Isogyres fringes visible. A polarizer (vertical, Fig. 2.42) and analyzer (horizontal) are introduced just before and after the Pockel Cell in a crossed position. Fine adjustment with precision gimbal mount (Fig. 2.43) is made to ensure that the crystal axis and the laser axis are collinear, which can be determined by isogyres seen on a screen as shown in Fig. 2.44 with laboratory He-Ne laser. After the two axes are made collinear, the variable diaphragm, diffuser and screen are removed to make the setup ready for the second phase of the experiment with RG shutter action.

To check the behaviour of the shutter when high voltage is applied to it, we

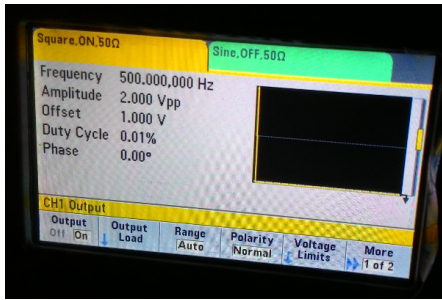


FIGURE 2.46: Function Generator.



FIGURE 2.47: Laser Metric: Pockel Cell controller.

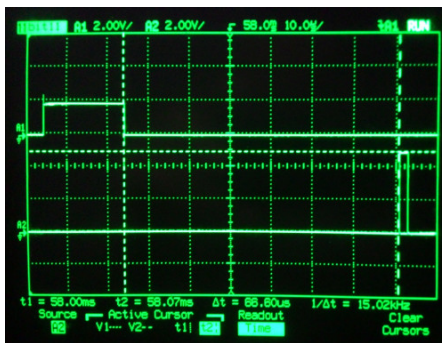


FIGURE 2.48: A1: function generator signal, A2: shutter ON signal, delay: 66.67 μsec .

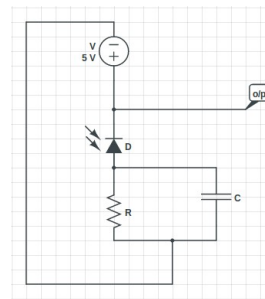


FIGURE 2.49: Photodiode in reverse bias.

triggered the delay generator (DG, Fig. 2.45) with a 500 Hz square signal from a function generator (as a dummy LGS laser signal, Fig. 2.46). The output ON/OFF signal from the DG triggers the ON/OFF state of the Pockels cell. The applied voltage on the Pockels cell is as high as 3 kV through the PC Controller (Fig. 2.47). The ON/OFF signals are separated by $\Delta t \sim 2.3 \mu\text{sec}$. (corresponding to 345 meter on the sky, which is the expected height of laser “spot”) whereas the time delay between the DG ON and the signal from the function generator (t_1 , shown in Fig. 2.48) is set to 66.67 μsec (corresponding to beam return time from 10 km altitude in the sky).

A sensitive photodiode (Hamamatsu, Si Photodiode (S238618K) in reverse bias (Fig. 2.49)) is used to pick up the gated signal from the Pockel cell, as shown in Fig. 2.50. The measured gate width is 2.68 μsec compared to a setting of 2.33 μsec

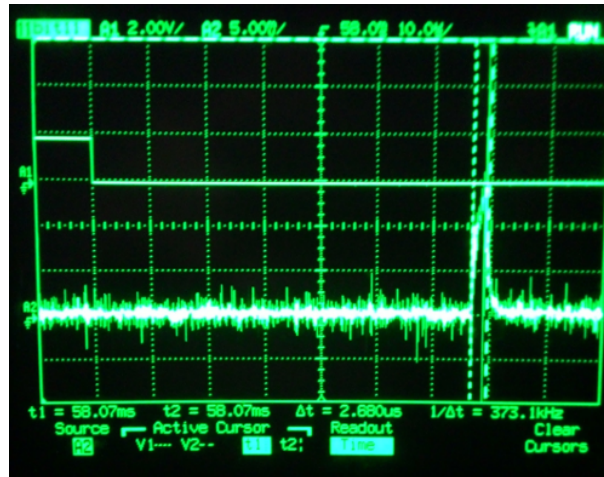


FIGURE 2.50: A gated pulse of width $2.3 \mu\text{sec}$ picked up by the photodiode using a function generator (time/major division: $10 \mu\text{sec}/\text{division}$).

2.3.5.5 Retarder -Half Waveplate/HWP

As the laser projector is located at the side of the telescope which has an Alt-Azm mount system, the Cassegrain derotator causes the polarization plane of the laser beam (as seen by the Pockels cell) to change with time. However, the Pockels cell works most efficiently when the plane of polarization of the input beam is aligned with respect to the axes of the crystal. To ensure that this happens an optical half wave plate retarder mounted on a rotating stage is introduced at the entrance of the range gate system. The retarder is rotated so as to align the plane of polarization of the input laser beam to the optimal direction once every 3 secs. The rate of rotation of the retarder is synchronized with that of the Cassegrain derotator. A single controller module drives the retarder mount as well as a pair of Atmospheric Dispersion Corrector (ADC, details of which is given in Section 4.6 of Chapter 4) prisms. A multi-threaded software has been developed to communicate with both mechanisms simultaneously.

Alt-Azimuth telescopes have a blind spot around the zenith, where observations are not possible. This is because, the azimuth axis will have to track at very high speeds near the zenith direction. The Zenith blind spot radius of the IGO 2m telescope is 2° . The set speed of the Half-wave plate is $2^\circ/\text{sec}$, which is sufficient to cope up with the change of the plane of polarization of the LGS up to 2° zenith angle.

As discussed earlier if χ is the angle by which the plane of polarization is to be rotated, then the HWP should be rotated by $\chi/2$ degree. There are three identical motorized rotational stages and all controlled by the same master controller. One of them is used for HWP, and the other two for the ADC prisms. Different algorithms govern rotations of the HWP and the ADC. A multi-thread program written in ‘C’ tackles both HWP and ADC simultaneously. The stand-alone HWP control flowchart is given in Fig. 2.51. It reads ‘retarder_offset.txt’ file for the offset of the rotating stage. It reads the telescope parameters which are stored in real time in the ‘tcs.txt’ file. The Cassegrain derotator’s value is taken from the ‘tcs.txt’ file and fed to the HWP controller to rotate it by half of that. The stage turns during the exposure time which is taken from the user through the ‘exposure.txt file.’

2.3.5.6 SHWFS

At the time of the initial phase of alignment, the SHWFS was mounted on a fixed custom made mount without any degrees of freedom for fine adjustment. But the mount had rotation, and this was noticed from the coordinates of the spots as seen in Fig. 2.52. The fixed mount was replaced by an off the shelf X-Y translating lens mount (Fig. 2.54) which allows x, y translation and rotation around the z-direction. Fig. 2.53 shows the rotation corrected array of spots. The next important step is arranging all the actuators as per Fried geometry. This demands that all the DM actuators are located at the corners of the lenslets. In this arrangement, each actuator influences the four adjacent spots equally. The co-location of DM actuators at the corners of the corresponding lenslet is achieved by translating the lenslet array in the XY plane. The positions of the actuators in the frame of reference of lenslet array are examined by poking a row or column of actuators along the diameter and peripheral actuators of the pupil. The numbering scheme of the 140 actuators and their relative positions in the DM are given in Fig. 2.25. The actuators are all poked to 40000 counts value⁹. But the differential poke count values from the flat map are different as the DM flat map counts are not identical. The poked values and the influence of it at the back focal plane of SHWFS lenslet array along a row and column are given in Figs. 2.55, 2.56, 2.57, 2.58. All the spots of two rows move towards a parallel line passing through the middle of both the influenced rows of spots. This line is the actuator line at DM.

⁹3.5 μm stroke is divided in 16 bit counts.

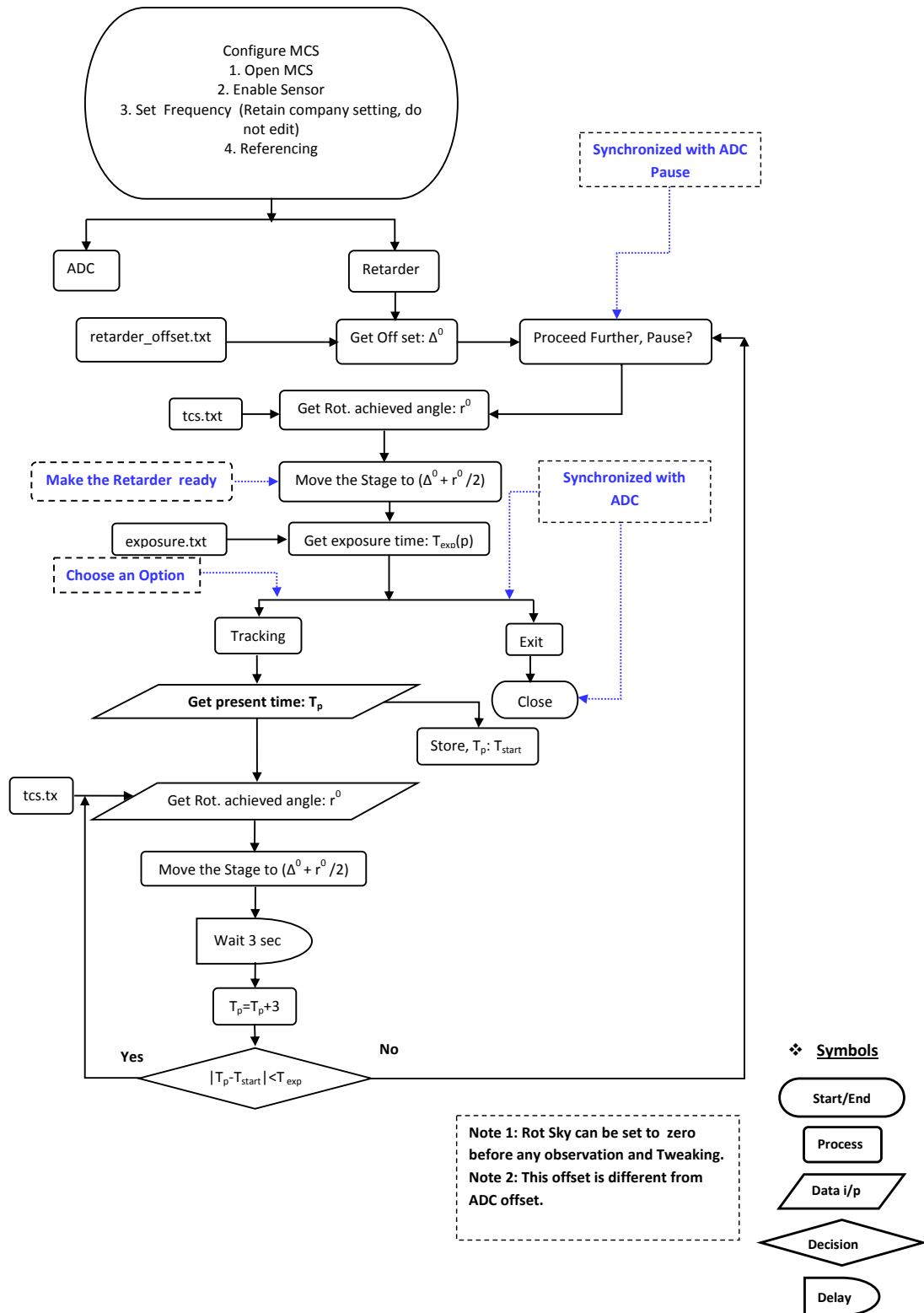


FIGURE 2.51: Half wave plate flow chart.

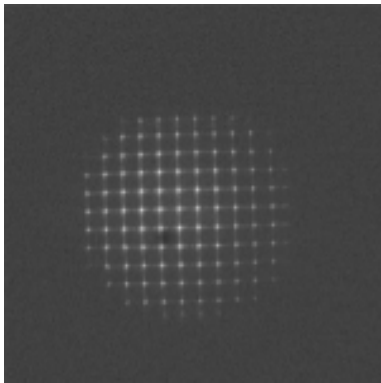


FIGURE 2.52: The rotated 11×11 array of UV spots at the back focal plane of the SHWFS due to the tilt in the SHWFS mount.

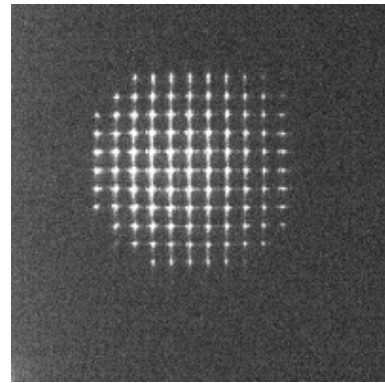


FIGURE 2.53: Rotation corrected array of UV spots at the back focal plane of the SHWFS, mounted in off the shelf X-Y translating lens mount.

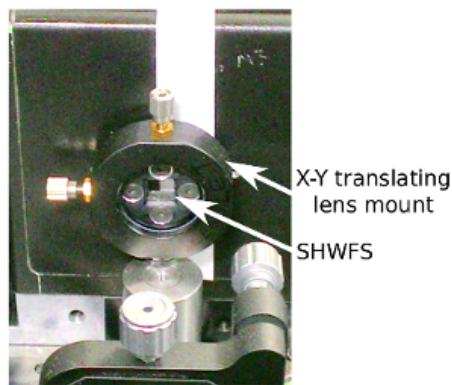


FIGURE 2.54: Lenslet array mounted on a X-Y translating and rotary lens mount.

Similarly, for the case of the column, actuators are along the vertical line passing through the middle of the two affected columns of spots. Finally, by poking all the peripheral actuators (Ex. 5, 24, 33, 59,70, 108, 117, 135), it is found that all the available spots adjacent to those actuators, shift radially (Fig. 2.59). Thus all the actuators are lies at the center of any four adjacent spots (2×2 array) i.e. at the corner of each lenslet.

2.3.5.7 Relay Lens

A couple of lenses are used to demagnify the 11×11 array of spots produced by lenslet array of size around 5.0×5.0 to fit in CCD39 of size 60×60 pixel, i.e. 1.44

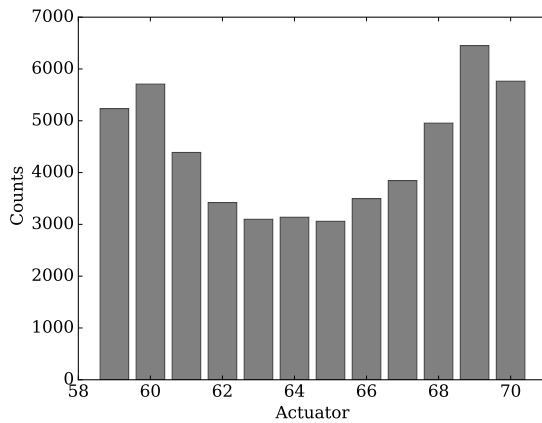


FIGURE 2.55: Counts of the poked actuators for a horizontal row with respect to the flat map of the DM.

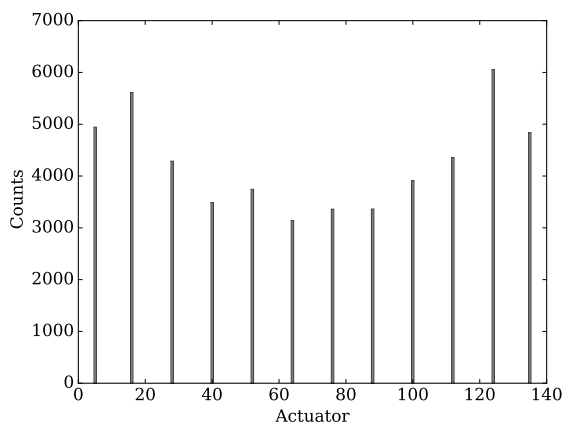


FIGURE 2.57: Counts of the poked actuators for a vertical column (5, 16, 28, 40, 52, 64, 76, 88, 100, 112, 124, 135 numbered actuators) with respect to the flat map of the DM.

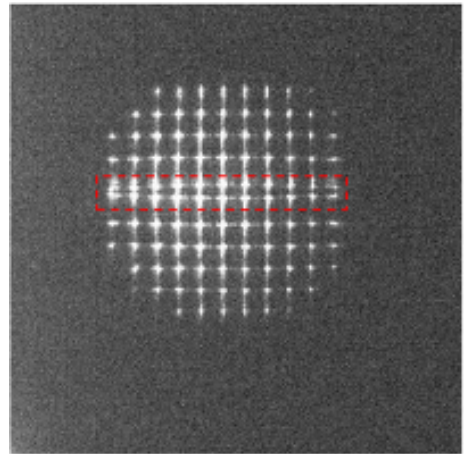


FIGURE 2.56: 11×11 array of UV spots at the back focal plane of the lenslet at ST9 camera (frame size: $1.92 \text{ mm} \times 1.92 \text{ mm}$) when 59 to 70 numbered actuators are poked, the influenced spots are marked within a rectangular dotted box.

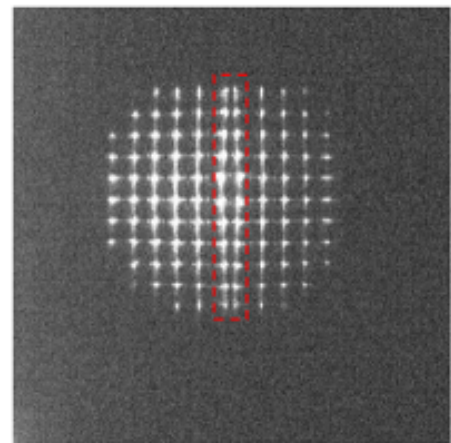


FIGURE 2.58: 11×11 array of UV spots at the back focal plane of the lenslet at ST9 camera (frame size: $1.92 \text{ mm} \times 1.92 \text{ mm}$) when 5, 16, 28, 40, 52, 64, 76, 88, 100, 112, 124, 135 numbered actuators are poked, the influenced spots are marked within a rectangular dotted box.

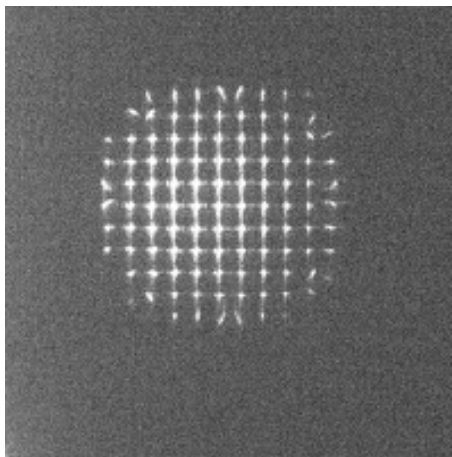


FIGURE 2.59: 11×11 array of UV spots at the back focal plane of the lenslet at ST9 camera (frame size: $1.92 \text{ mm} \times 1.92 \text{ mm}$) when the peripheral 5, 24, 33, 59, 70, 108, 117, 135 numbered actuators are poked, the influenced spots are visible in circumference.

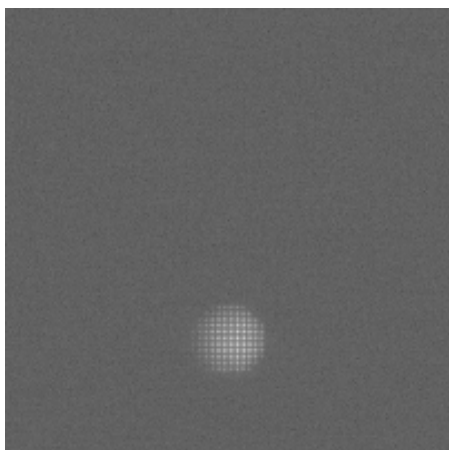


FIGURE 2.60: 11×11 array of UV spots at ST9 after relay lens system (frame size: $10.24 \text{ mm} \times 10.24 \text{ mm}$).

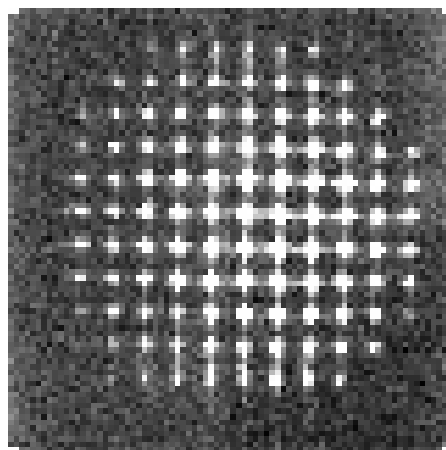


FIGURE 2.61: 11×11 array of UV spots at CCD39 after relay lens system (frame size: $1.92 \text{ mm} \times 1.92 \text{ mm}$).

$\text{mm} \times 1.44 \text{ mm}$. Result of the relay lens system is captured in ST9 camera given in Fig. 2.60 after demagnification.

2.3.5.8 CCD39

Scimeasure CCD39 is used for WFS camera. It has an 80×80 pixel array. Each of the spots is placed at the centre of a 6×6 pixel box. Fine alignment of the spots with CCD pixels is done by adjusting the last relay lens. The 11×11 array

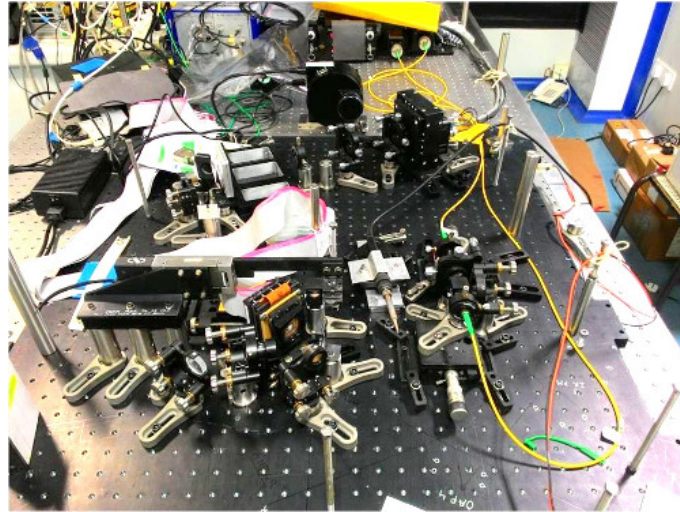


FIGURE 2.62: A photograph of the entire UV arm with elliptical mirror and telescope simulator except the range gate.

of UV spots as captured on CCD39 is given in Fig. 2.61. Each of the 6×6 pixel box is binned 3×3 to reduce it to a quad cell of 2×2 pixels. The centroids of each spot is determined using the quad cell formula.

Fig. 2.62 shows a photograph of the assembled UV arm along with components that are common with the other arms.

2.3.6 Visible/NIR arm

2.3.6.1 OAP2 and OAP3

The visible and near-infrared collimated beam transmitted through the laser dichroic is incident on OAP2 which converges the light. OAP3 then collimates the emerging beam and forms a pupil at the Atmospheric Dispersion Corrector (ADC). The light from all field points encounter the same glass thickness at this pupil. Fig.2.63 shows the circular collimated spot of diameter 9.5 mm. The shearing interferometer output showing straight line fringes along the shearing direction (Fig.2.64) demonstrates the collimation of the beam. The design considerations and system description of the ADC is dealt with in detail in Chapter 4.

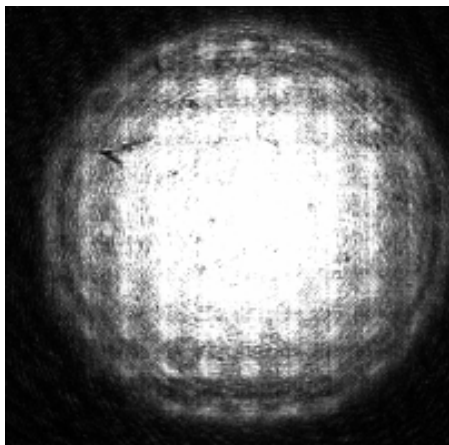


FIGURE 2.63: Visible collimated beam produced by OAP3.

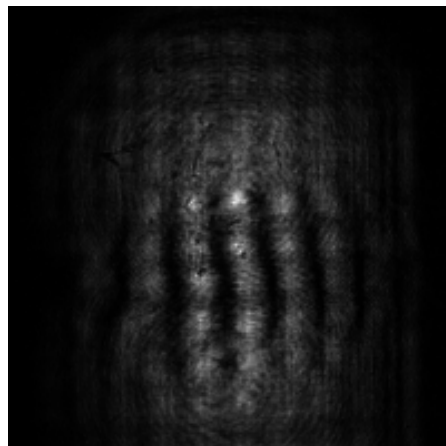


FIGURE 2.64: Examination of the quality of collimation of the visible beam produced by OAP3 in shearing interferometer.



FIGURE 2.65: TTM platform, with test mirror attached

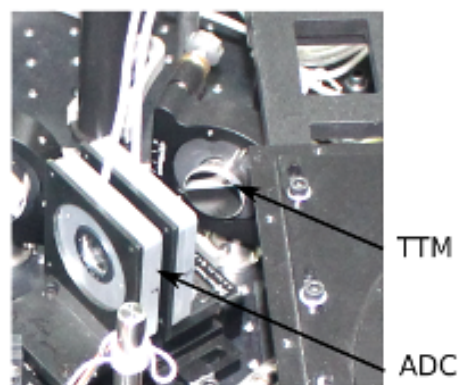


FIGURE 2.66: The position of the glued TTM on the tip-tilt platform in visible/NIR arm after alignment.

2.3.6.2 Tip-Tilt Mirror (TTM)

The Tip-Tilt Mirror (TTM) is used to correct the tip-tilt aberration which is the lowest mode and has the highest power, so as to reduce stroke requirement of the DM, as discussed earlier. The mirror is mounted on a tip-tilt platform (Fig. 2.65). During the alignment (Fig. 2.66) it is ensured that there is no obscuration to the extreme field points from any component like ADC, OAP4 etc.



FIGURE 2.67: FW1 populated with visible Bessel U, B, V, R and I filters with an empty slot.

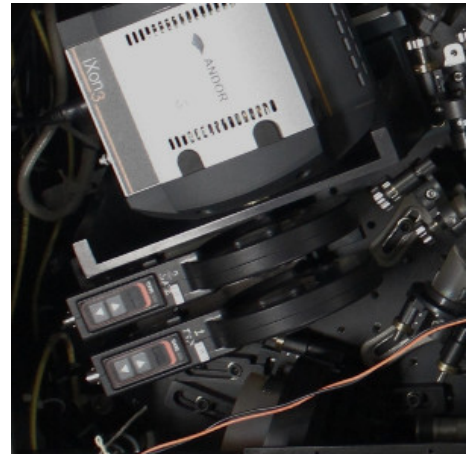


FIGURE 2.68: Filter wheels assembly in front of Andor EMCCD camera.

TABLE 2.5: Filter Wheels.

| FW No | Slot 1 | Slot 2 | Slot 3 | Slot 4 | Slot 5 | Slot 6 |
|-------|--------|--------|--------|--------|--------|--------|
| FW1 | U | B | V | R | I | Empty |
| FW2 | Empty | Unused | Unused | Unused | Unused | Dark |

2.3.6.3 Filter Wheel(FW)

At present, five (U, B, V, R and I) visible band Bessel filters are placed in one of the two filter wheels (Fig. 2.67) and given in Table 2.5. There are six slots on each wheel. One slot is always empty on each filter wheel so a filter on either wheel can be inserted into the beam. A light blocking aluminium plate is placed in a slot of the second filter wheel for taking dark frames. The remaining four ‘Unused’ slots are free for future use of other filters. Both filter wheels are mounted just in front of the visible Andor EMCCD camera shown in Fig. 2.68.

2.3.6.4 OAP4, Science Dichroic and Andor EMCCD camera

The OAP4 is the final optical element of the visible arm that make the final image on the EMCCD camera while meeting the sampling requirements. Fig. 2.69 shows the system at the end of the visible/NIR arm alignment. The final f-number is around $f/45.6$.

The beam is folded and split between visible and near-infrared bands by a science dichroic. It reflects visible light towards Andor EMCCD camera and transmits

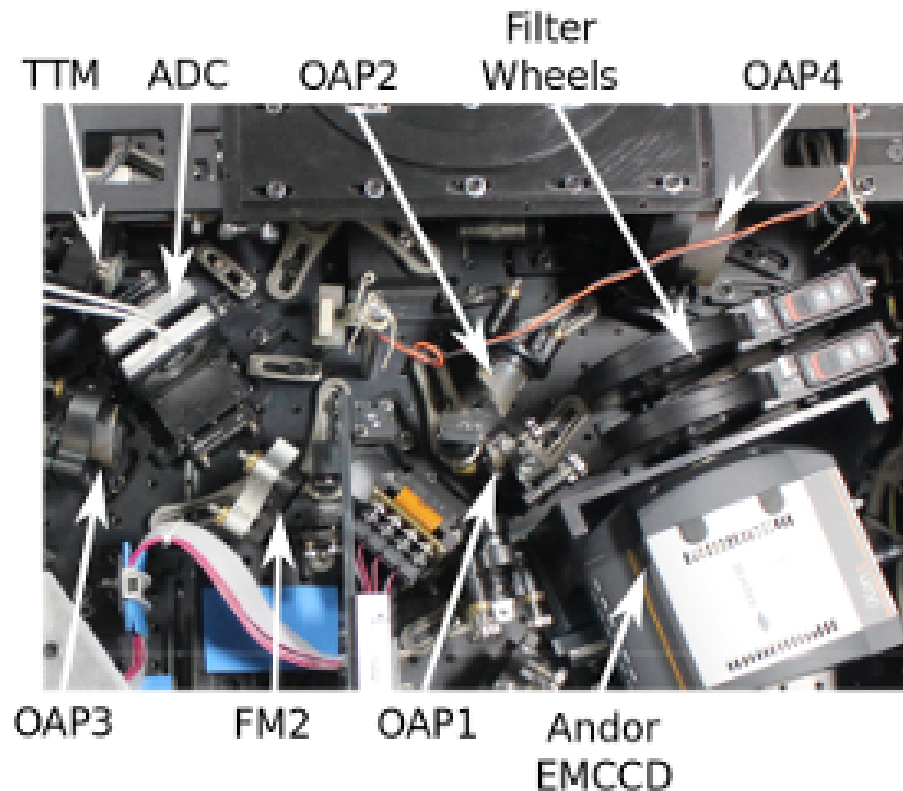


FIGURE 2.69: Bread board at the end of Visible/NIR arm integration.

near-infrared light. The transmitted near-infrared light forms AO corrected NIR focus. The science dichroic is aligned keeping the on-axis $f/45.6$ beam at its centre and reflects the visible beam to form the image at the centre of the Andor EMCCD camera. The position of the science dichroic is shown in the optical layout, Fig.2.4.

An image at the EMCCD Andor camera is shown in Fig. 2.70 when both the DM and TTM are ON and initialized, i.e. the DM is loaded with the flat map. 2D and radial plot of the PSF are shown in Fig. 2.71 and 2.72 respectively using Image Reduction and Analysis Facility (IRAF) software. The FWHM is around 4 pixels which is larger than the Zemax optimized spot size of 2.36 pixels as shown in Fig. 2.73. The broadening of the spot with respect to the Zemax prediction is due to defocus, the finite size of the fiber tip in the telescope simulator and any residual aberrations in the optical alignment. In the telescope, the linear translation of the secondary mirror can be used for focusing. As the f /number is high, the defocus will not change the plate scale of the camera, and it behaves like an image space telecentric system.

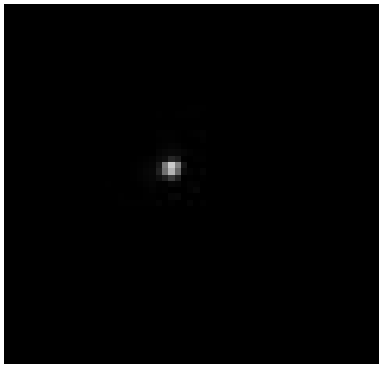


FIGURE 2.70: Final Image at ANDOR.

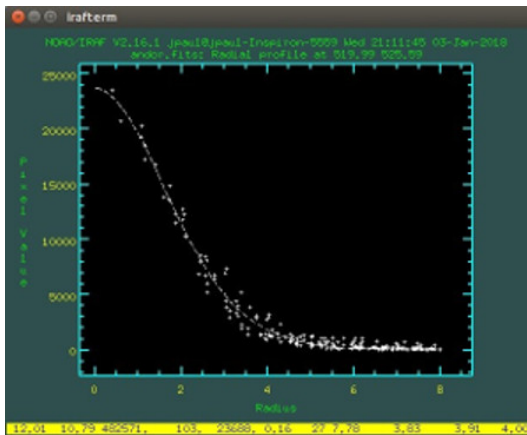


FIGURE 2.72: Radial profile of Andor spot, while DM (flat) and TTM are under initialized/nominal condition, FWHM ~ 4 pixel.

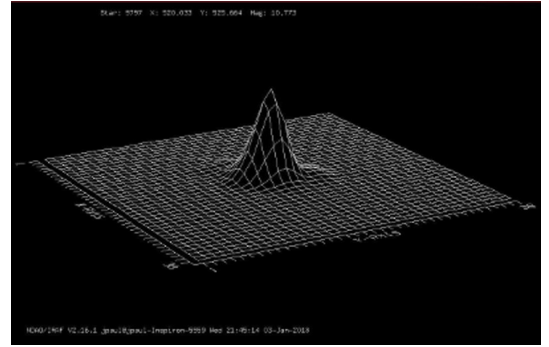


FIGURE 2.71: ANDOR 2D Spot, under DM Flat and TTM initialized condition.

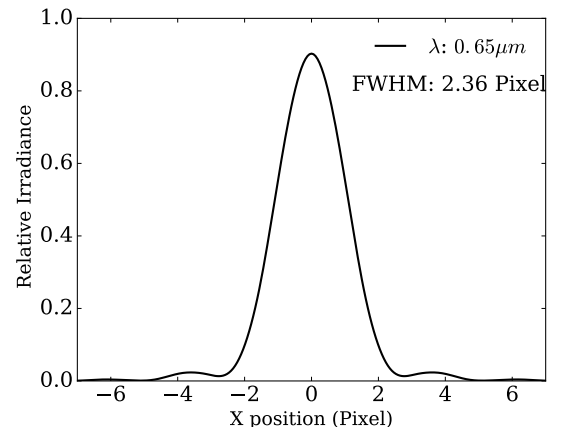


FIGURE 2.73: FFT PSF cross-section of the on-axis visible spot at Andor in $0.65 \mu\text{m}$ as per Zemax.

Andor EMCCD camera of $1k \times 1k$ (1MHz-16bit for single mode acquisition and 10MHz-14bit for rapid frame acquisition) pixels is aligned normal to the optic axis keeping the on-axis object (i.e. telescope simulation visible spot) at the centre of the frame.

At the end of the complete optical integration assembling, the iRobo-AO Cassegrain AO facility is shown in Fig. 2.74, identical in orientation with the optical layout (Fig.2.4) and mechanical CAD model (Fig. 2.5) respectively.



FIGURE 2.74: Fully assembled iRobo-AO Cassegrain box.

2.4 Optical Performance:

With an $f/45.42$ beam and a plate scale $2.25''/\text{mm}$ at the input of the EMCCD, a theoretical estimate of the FWHM at $\lambda = 0.65 \mu\text{m}$ is $\sim 30.4 \mu\text{m}$ or 2.34 pixels, which satisfies the Nyquist criteria. Fig. 2.75 shows the polychromatic spot diagram on the EMCCD for a total FOV of $\pm 15''$. The variation of the RMS spot size at EMCCD as a function of field position is given in Fig. 2.76.

In the UV arm the most important parameter other than the pupil diameter on the SHWFS is the wavefront error and the degree of collimation of the beam. After several rounds of iteration of the lens (after UV dichroic) and OAP5 parameters we obtain a $0.5''$ collimated beam with a tilt removed P-V and RMS wavefront error of 0.04λ and 0.0072λ at $0.355 \mu\text{m}$.

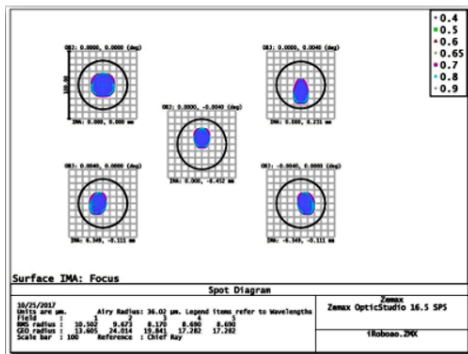


FIGURE 2.75: Polychromatic spot diagram on EMCCD.

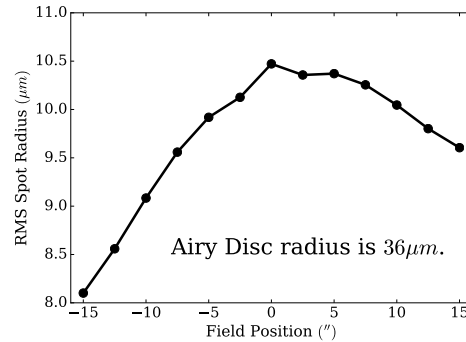


FIGURE 2.76: RMS spot size variation at EMCCD with field position.

2.5 Heat Exchanger (HE)

The Pockel cell requires water cooling to safely operate without the crystals getting heated up, beyond a shutter speed of 1kHz. Similarly, in order to cool the EMCCD over 100°C below ambient, water cooling is required. A heat exchanger supplies cold water to both the components. Water cooling arrangement for Pockel cell and Andor camera is given in Fig. 2.77. A flow meter is connected at the cold water outlet of the heat exchanger to measure the rate of water flow. A ‘T’ connector bifurcates the flow meter outlet. These cool water lines are connected to Andor EMCCD and the pockel cell, respectively. The outlet water lines from the two individual components are merged together using a ‘T’ connector and return the hot water to heat exchanger for cooling.

2.6 Electronic Rack

There are several electronic controllers which need to be located near the Cassegrain AO box. The Cassegrain box controllers are mounted on the eight side ports of the telescope (Fig. 2.78) at the Cassegrain derotator. The names of all controllers and their locations on the telescope are given in Table 2.6.

The electrical connections among all the components with their respective controllers and computers are illustrated in Fig. 2.79. This representation of cable layout is adapted from Robo-AO cable layout, which was originally developed by Mahesh P. Burse, IUCAA, Pune.

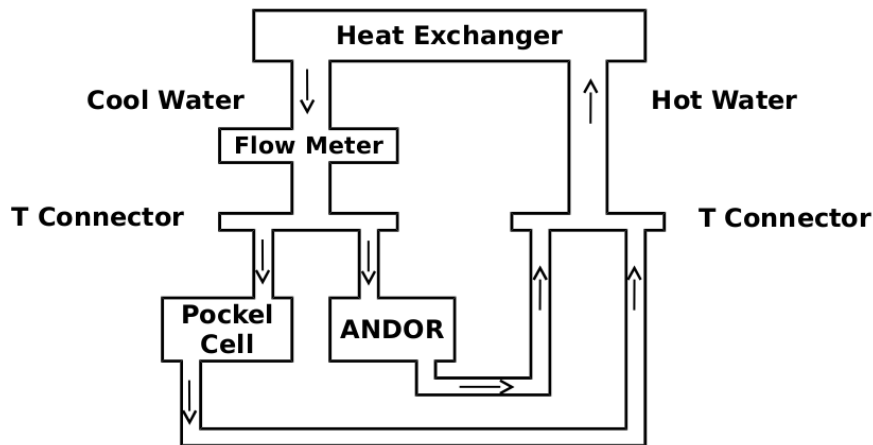


FIGURE 2.77: Heat exchanger water cooling arrangement for Pockel cell and Andor camera.

TABLE 2.6: Side port wise name of controllers/components.

| Port Name | Components Name |
|-----------|--|
| Port A | DM Controller, DM PS, Smaract PS, Smaract Controller, HE, Flow Meter |
| Port B | TTM Controller (4 channel) |
| Port C | Scimeasure Controller, Scimeasure PS, RG Controller, Adam module($\times 4$), Adam module PS, DG |
| Port D | Preoccupied by CCU unit |
| Port E | Telescope Simulator Controller ($\times 2$) and preoccupied by Auto Guider |
| Port F | Preoccupied by Power House and Auto Guider Controller |
| Port G | iRobo-AO, SmarAct CPU and network hub |
| Port H | NPS* ($\times 3$) and preoccupied by Acquisition Guiding |

Note: PS stands for Power Supply, DC adapter

There are main three blocks - Electronic rack, Cassegrain box and Laser projector box in the electrical layout. The Electronic rack is further divided into two parts, i.e. Cassegrain box controller and Laser projector controller. The connections can be divided into four types, as marked in Fig. 1.79, considering the terminal blocks.

- Electronic Rack to Electronic Rack (E2E)
- Electronic Rack to Cassegrain Box (E2C)
- Cassegrain Box to Cassegrain Box (C2C)
- Laser Projector Box to Electrical Rack (L2E)

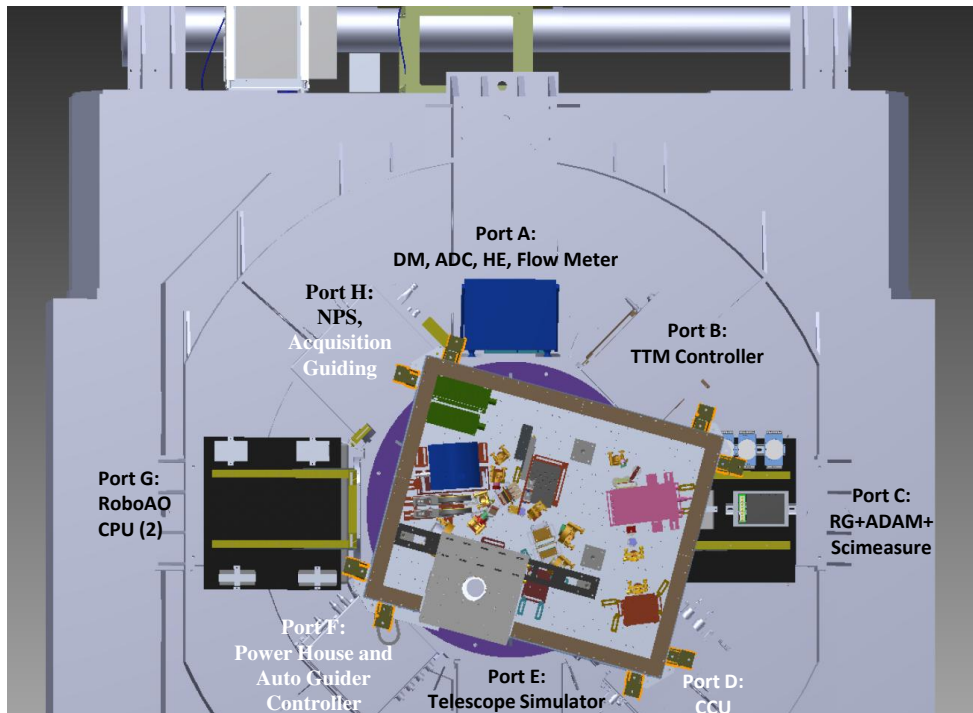


FIGURE 2.78: Location of iRobo-AO controllers at the side ports of telescope.

There is also colour coding in each connection based on its terminal hardware (controller/component head), and functionalities, which helps to identify any cable instantly.

These are given below.

- Controller to controller/component head connections are expressed in the green line.
- The power lines are indicated with the red line with an alphanumeric number ('np') assigned to each connection to distinguish and identify explicitly, where 'n' is number and 'p' stands for power.
- Computer connections with all the electronic gadgets are marked with the blue line.
- The black line is dedicated to the representation of all the network connections to have the remote control of the entire system.

During the initial installation the Network Power Switch (NPS) and the Weather Sensor Adam module have not been fully integrated. These will be made operational in future.

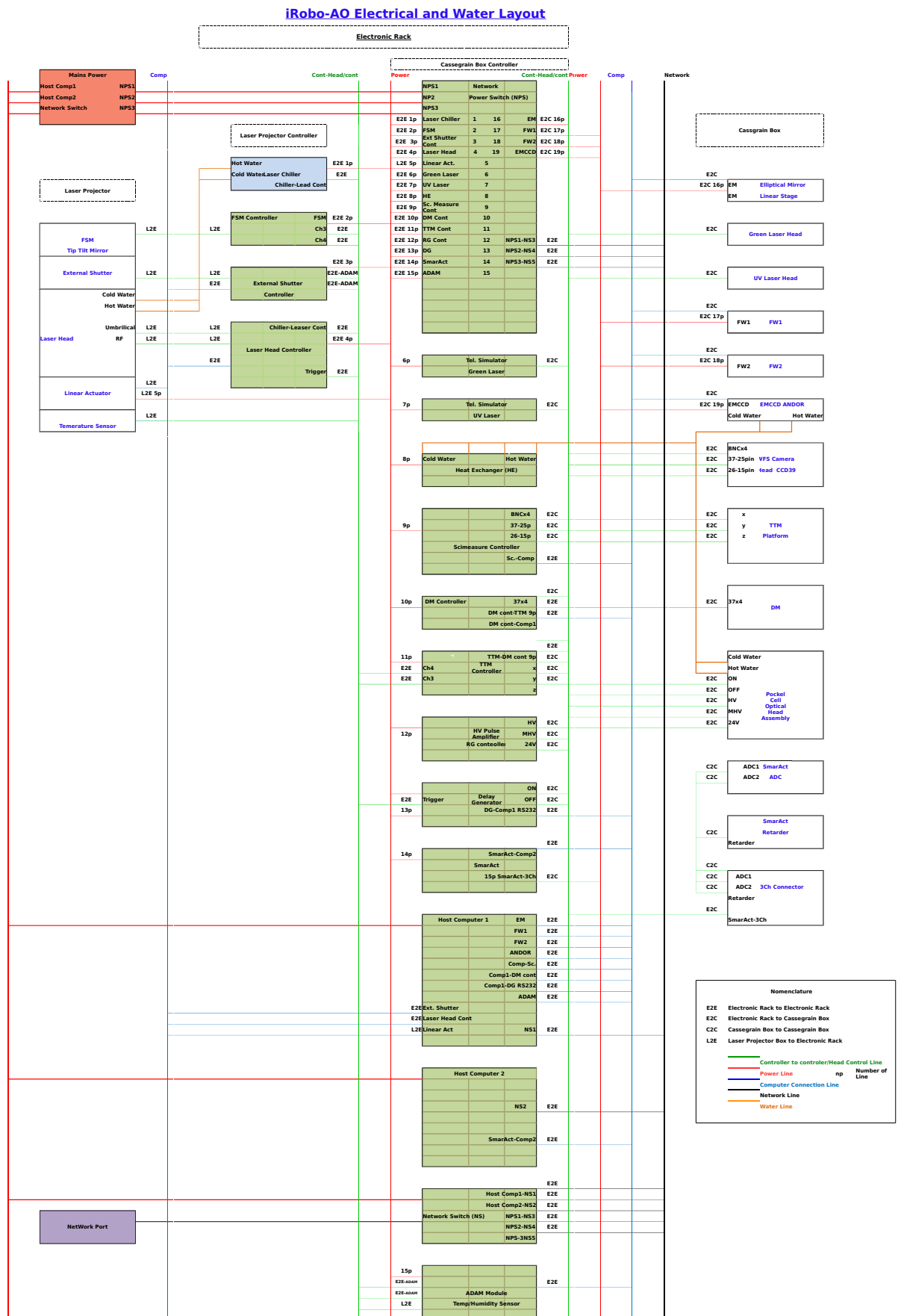


FIGURE 2.79: Electrical and water layout.



FIGURE 2.80: Panel1A.

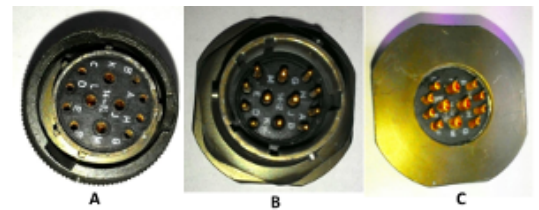


FIGURE 2.81: DC power patch adapter, (a) on cable part (b) and (c) are both ends of the panel part of the adapter.



FIGURE 2.82: Panel1B.



FIGURE 2.83: Panel2

2.6.1 Electrical Panels

The various controllers are grouped into four panels so that they are located as close as possible to the subsystems within the Cassegrain AO box which they control. These are given below.

- Panel 1A (Fig. 2.80) contains Andor, Smaract (for ADC and Retarder-Halfwave plate), Adam module (weather sensor), TTM (channel 1, channel 2 and channel 3), Filter wheels (FW1 and FW2), DM (J1, J2, J3, J4) and DC patch adapter (Fig. 2.81) for DC power service for Andor and filter wheel. The pin connection for the DC patch adapter is given in Table 2.7.
- Panel 1B (Fig. 2.82) hosts only the controller of the motorized linear actuator (Newport Conex) of elliptical fold mirror (FM1).

TABLE 2.7: DC Patch Adapter Pin Connection.

| Pin Number | Component |
|------------|--------------------|
| A | Filter Wheel 1 +ve |
| B | Filter Wheel 1 -ve |
| G | Filter Wheel 2 +ve |
| H | Filter Wheel 2 -ve |
| J | Andor +ve |
| K | Andor -ve |

- Panel 2 (Fig. 2.83) has Pockel cell (on, off, 24v, bias and high voltage) and CCD39 connections [25 pins, 15 pins and four-channels for CCD readout connection (red, green, blue and black)]
- Panel 3 Visible and UV laser of simulator.

2.7 Software Architecture

The iRobo-AO software is adapted from the original Robo-AO[85]. The entire software was developed in C++ running on a PC with Linux Fedora 13 operating system. The software is built in a very modular fashion with respect to the different hardware components. The various software modules are listed below.

- Wavefront Sensor (WFS) camera (CCD39)
- Deformable Mirror (DM)
- Tip-Tilt Mirror
- Tip-Tilt Camera
- Laser System (laser, laser chiller, safety shutter, beam steering mirror(FSM), range gate)
- Atmospheric Dispersion Correction system
- Visible Camera
- Infrared Detector
- Filter Wheels

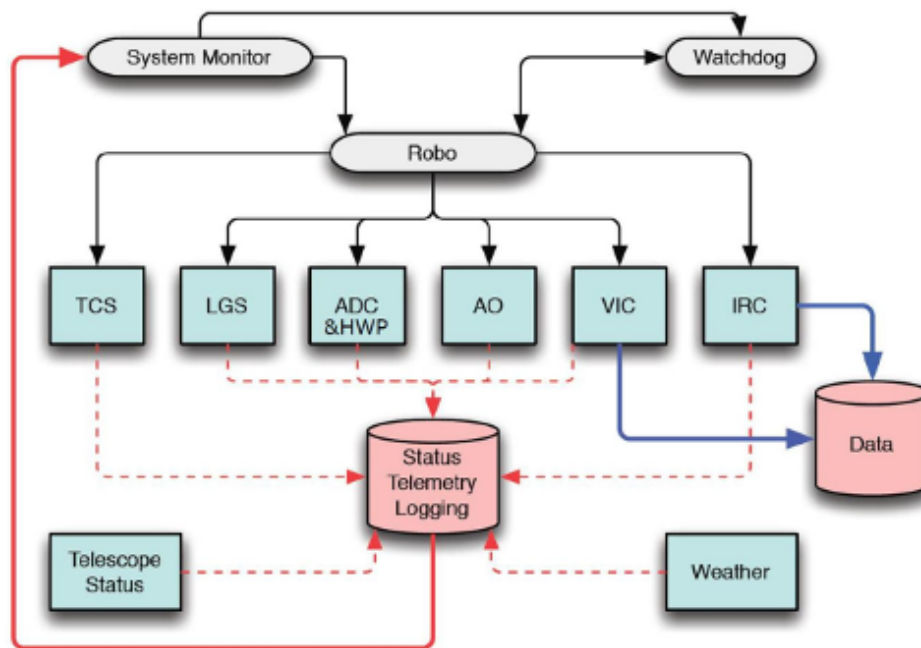


FIGURE 2.84: Software Architecture of Robo-AO System. The hardware control subsystem daemons are represented in blue boxes; grey coloured boxes are control or oversight daemons and red boxes are for data file storage. The different paths shown in the picture display the telemetry, command and data paths (Fig. 2 of [85]).

- Network Power Switch (NPS)
- Telescope operations and monitoring

The above set of hardware subsystems are assembled together and controlled through a set of software daemons as listed below and illustrated in Fig. 2.84.

1. Adaptive Optics (AO): It controls the WFS CCD39, DM, tip-tilt mirror system, laser beam steering mirror (FSM) and adaptive optics functions.
2. Laser Guide Star (LGS): Controls the laser projector hardware operation with the external laser safety shutter.
3. ADC and Half waveplate (HWP): It operates the subsystem that corrects for atmospheric dispersion (given in chapter 4) and derotates the polarization of LGS. This software was developed specifically for iRobo-AO and was not part of the original Robo-AO software.

4. Visible Instrument Camera (VIC): It controls the visible science camera-EMCCD and filter wheels.
5. InfraRed Camera (IRC): Operates the infrared science system, including the detector and filter wheels, homing, thermal sensors etc. IRC is under development, and a brief discussion is given in chapter 5.
6. Telescope Control System (TCS) interfaces with the telescope system to command the telescope operations from the Robo-AO software platform itself. This is again IGO specific.
7. Telescope Status : Monitors telescope status. It is another IGO specific software component.
8. Weather: It collects weather condition information (temperature, humidity) from the Laser projector and Cassegrain Box.

The robotic software system is not fully integrated at the moment . This will be done in a future commissioning run.

2.8 New Features:

The entire instrument is optimised for IUCAA 2 m Alt-azimuth system at Cassegrain main port. In the process, all the major optical components had to be redesigned to meet the iRobo-AO requirement as given in Table 2.4. The incorporation of retarder in front of the Pockel cell and the introduction of a generic atmospheric parameter sensitive ADC software (given in chapter 4) are new additions to the system.

2.9 Wavefront Reconstruction

The DM, SHWFS and the WFS camera are aligned as per the geometry shown in Fig. 2.85. The output of the WFS camera is a 3×3 binned image of 26×26 binned pixels. There are 13×13 subapertures on an image, out of which only 11×11 subapertures are within the pupil and among them only 97 subapertures are used for the AO correction. The rest are unused because they do not contribute

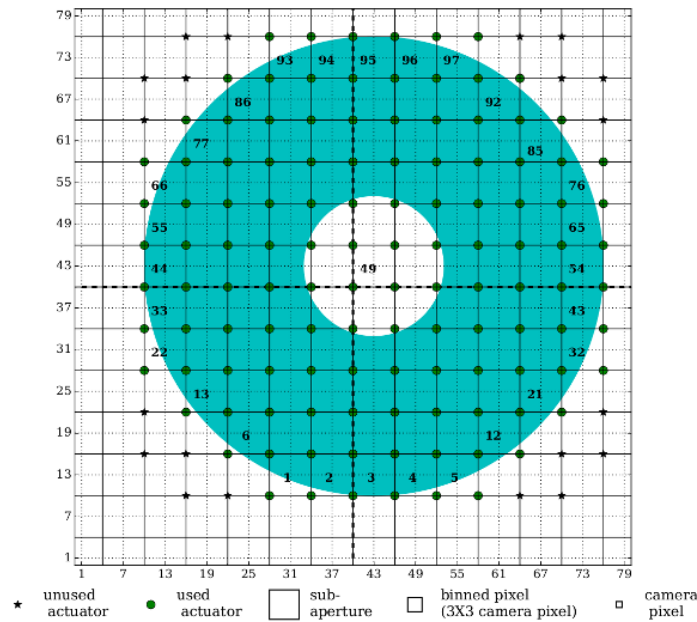


FIGURE 2.85: Mapping of DM actuators and SHWFS lenslets as seen on WFS camera, the annular region represents the pupil size with secondary obscuration and each subaperture consists of 2×2 binned pixels. One binned pixel consists of 3×3 camera pixels.

in wavefront sensing over the annular pupil. Each subaperture consists of 2×2 binned camera pixels. An unbinned image of the spot array formed by the SHWFS lenslets as seen on the WFS camera is shown in Fig. 2.86 after complete alignment of the wavefront sensing arm. Fig. 2.87 depicts the control structure of iRobo-AO.

From each new image grabbed by the WFS camera, a linear array of pixel values are formed from which the wavefront slopes are measured. The x and y slopes of the images within each subaperture are calculated as [3]

$$S_x = \frac{(I_2 + I_4) - (I_1 + I_3)}{(I_1 + I_2 + I_3 + I_4)} \quad (2.26)$$

$$S_y = \frac{(I_3 + I_4) - (I_1 + I_2)}{(I_1 + I_2 + I_3 + I_4)} \quad (2.27)$$

where the intensity in each binned pixel is numbered in a quadrant cell format as

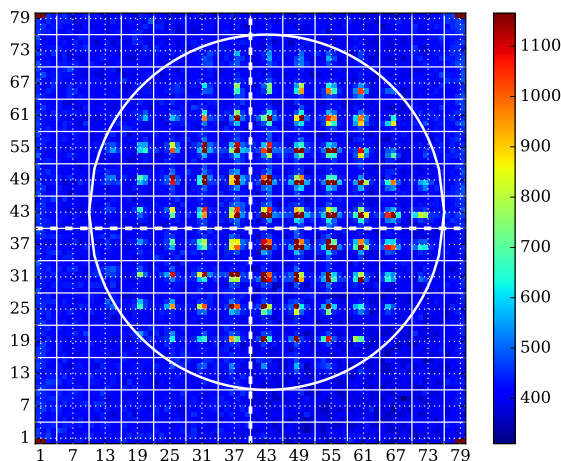


FIGURE 2.86: Unbinned image of the spot array formed by SHWFS lenslets as seen on the WFS camera, the squares (solid line) and circle are representation of the subapertures and the telescope pupil.

$$\begin{pmatrix} I_3 & I_4 \\ I_1 & I_2 \end{pmatrix} \quad (2.28)$$

As the response of a quadrant cell is nonlinear in nature, particularly when the spot reaches the edges, the slopes are first linearized with the help of a pre-calculated table. Non-common path errors are taken care of with the help of slope offsets, where again all the slope offsets are stored in a pre-calculated table. The final slopes are then multiplied by the reconstruction matrix to generate new DM actuator poke voltages as per the control law:

$$P(t+T) = P(t) + gE(t) + l[F - (P(t) + gE(t))] \quad (2.29)$$

where, $P(t+T)$ denotes the new position of the DM actuator, $P(t)$ denotes the current position of the DM actuator, $E(t)$ denotes the errors after matrix multiplication and F is the flatmap values of the DM describing its flat position. g and l are the loop gain and leak constant[86]. For small l , and in the absence of any measurement error, the system has a very small tendency to fall back to the flatmap values.

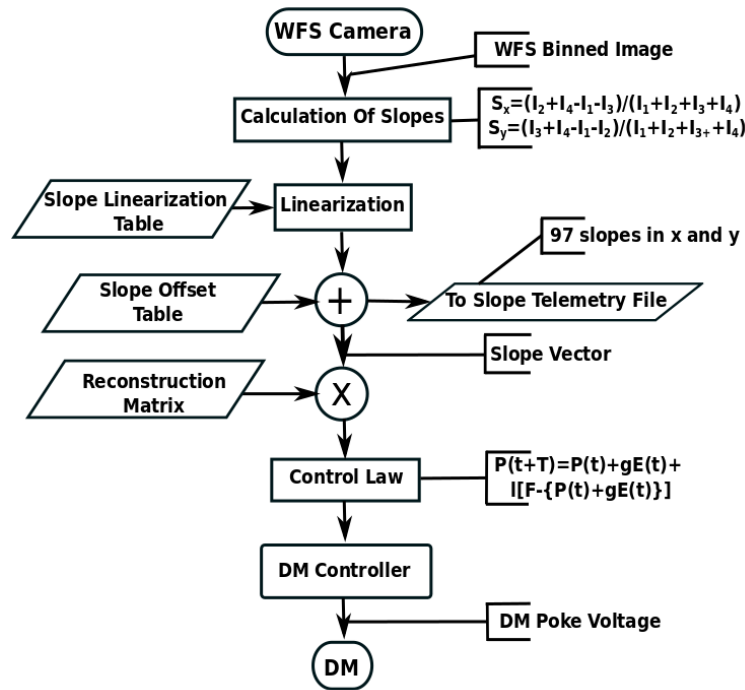


FIGURE 2.87: iRobo-AO Wavefront Reconstruction and DM signal generation flow chart.

2.9.1 AO loop

Here we test the performance of the AO system by comparing the residual slopes measured by the WFS when the system was run (1) without and (2) with the AO closed loop turned On. The local X and Y slopes of the spots within each subaperture of the binned image were estimated and stored in the slope telemetry file (Fig. 2.87). This was done for all the 97 subapertures and in all the image frames captured within the specific runtime.

Fig. 2.88 shows the rms values of a set of 97 slopes against the individual frame numbers for both the cases, when AO correction was (i) absent and (ii) present. We present the data from three test runs in Fig. 2.88. In Table 2.8 shown are the mean of slope RMS and the standard deviation of the data plots in the linear sections for all cases.

Case (i), panel (a) of Fig. 2.88 shows the rms variation of X and Y slopes when there is no AO correction. Mean of slope rms of X and Y slopes are 2.894×10^{-1} and 2.635×10^{-1} respectively.

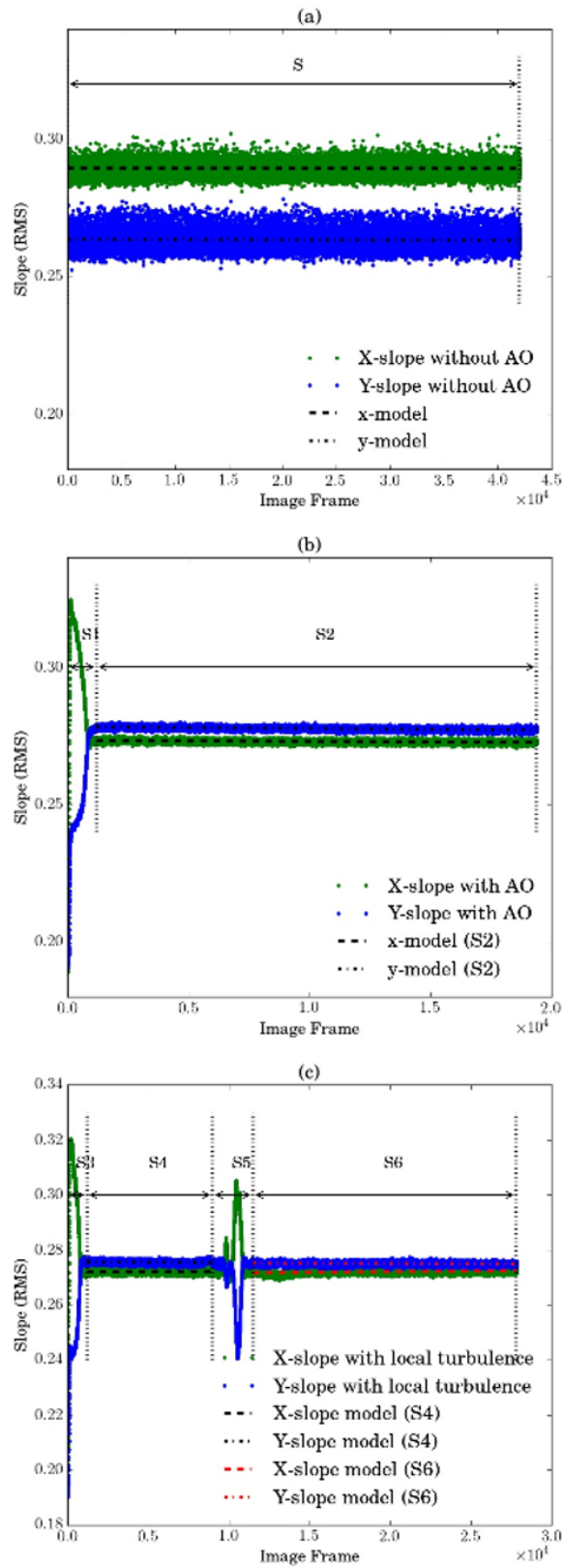


FIGURE 2.88: Panels (a), (b) and (c) represents the RMS variation of the slopes (dimension less) with image frames in the absence AO correction, the presence of AO correction and presence of AO correction under artificial turbulence respectively.

Case (iia), panel (b) of Fig. 2.88 shows the rms variation of slopes when the AO loop correction was turned on. The entire time plot is divided into two parts, the initial system transient (S1) and steady-state part (S2), as shown in Fig. 2.88. We can see the servo effect, i.e. oscillation at the beginning of the system (transient state) during the S1 segment. The RMS value in the transient was drastically reduced within the first few thousand frames. Then it reaches the steady state resulting in a flat curve (mean of slope rms of X and Y slopes are 2.733×10^{-1} and 2.782×10^{-1} respectively in S2 segment). As a result of the servo loop state transition, the system is trying to achieve the target value from an off condition through the transient. Once the system reaches the target state, it locks and does not deviate from the target value. Thus standard deviation reduces in locking period. Comparing Figs. 26a, 26b and results from Table 2.8, we find more than 70% reduction in slope deviation in X and Y, also the relative shift between mean of X and Y slope RMS in Fig. 26b is less by 80% as compared to Fig. 26a.

Case (iib) panel (c) of Fig. 2.88, depicts the system performance when artificial turbulence was introduced in the beam path, by passing ~ 1 Ampere current through a 5 Watt resistance. It was mounted at a location such that the local turbulence generated from heating of the resistance would disturb the collimated light in the path of the telescope simulator. This disturbance would be reflected as a severe shift of slopes on the WFS camera. After the AO loop ran for some time; the heater was switched on for a period of about 5-10 secs. only. The entire time plot is segmented into four parts S3, S4, S5 and S6.

Here S1, S3 represents the system's initial transient and steady parts. S5 represents the turbulent zone generated due to heating of the resistance. S2, S4 and S6 are the corrected segments.

Servo oscillation is present at the beginning of the system at the S1 segment which is brought down by the system within first thousand frames similar to the panel (b). The region where the artificial turbulence begins is distinct and shows high disturbance of the slopes in segment S5, eventually, this effect was also nullified quickly as we can see that the fall of the slopes (in segment S6) due to the AO correction.

TABLE 2.8: Statistics of data points in the linear sections

| Panel | Segment | Slope* | Mean of Slope RMS | Standard Deviation |
|----------------------------|---------|---------|------------------------|------------------------|
| (a) without AO | S | X-Slope | 2.894×10^{-1} | 2.137×10^{-3} |
| | | Y-Slope | 2.635×10^{-1} | 2.832×10^{-3} |
| (b) with AO | S2 | X-Slope | 2.733×10^{-1} | 5.668×10^{-4} |
| | | Y-Slope | 2.782×10^{-1} | 6.181×10^{-4} |
| (c) with AO and turbulence | S4 | X-Slope | 2.721×10^{-1} | 5.330×10^{-4} |
| | | Y-Slope | 2.757×10^{-1} | 5.927×10^{-4} |
| | S6 | X-Slope | 2.711×10^{-1} | 6.325×10^{-4} |
| | | Y-Slope | 2.753×10^{-1} | 5.674×10^{-4} |

* Slope is dimensionless as per the Equation 2.26, 2.27.